Constraining the quenching mechanisms of galaxy clusters through the evolution of stellar mass functions within GOGREEN and GCLASS

by

Guillaume Hewitt

A thesis
presented to the University of Waterloo
in fulfilment of the
thesis requirement for the degree of
Master of Science
in
Physics

Waterloo, Ontario, Canada, 2024

© Guillaume Hewitt 2024

Author's Declaration

This thesis consists of material all of which I authored or co-authored: see Statement of Contributions included in the thesis. This is a true copy of the thesis, including any required final revisions, as accepted by my examiners.

I understand that my thesis may be made electronically available to the public.

Statement of Contributions

I hereby declare that I am the sole author of this thesis, which was written under the supervision of Michael Balogh.

The data used within this project was obtained, reduced, and catalogued by the GOGREEN collaboration as published in Balogh et al. (2021). The additional cluster SpARCS-1033 was reduced and catalogued by Florian Sarron.

Figure 1.1 is from Klypin et al. (2016), Figure 1.2 is from Wechsler & Tinker (2018), and Figure 5.1 was adapted from Papovich et al. (2018).

All other work in this thesis is my own.

Abstract

We present an analysis of the stellar mass functions (SMFs) of 17 rich galaxy clusters within the GOGREEN and GCLASS surveys in the redshift range of $0.8 < z < 1.5$, down to a stellar mass limit of $\log(M/M_{\odot}) = 9.5$. We fit all the data simultaneously with a model that allows the Schechter function parameters of the quiescent and star-forming populations to vary smoothly with radius and redshift. The model also fits for the concentration parameter of each population, and the quenched fraction is modeled as a smooth function of redshift and velocity dispersion. We fit the data in a Bayesian manner, using MCMC. We find no significant dependence of the shape of the star-forming SMF on radius nor redshift, and find it to be consistent with the field. We confirm previous results of a radial dependence on the quenched fraction. We find a moderately significant radial dependence on the α and M^* parameters of the quiescent population SMF. The cluster core has a highly elevated quenched fraction, yet the core quiescent SMF is more similar in shape to the quiescent field. The cluster non-core has an moderately elevated quenched fraction, and its quiescent SMF is more similar to the shape of the star-forming field. We explore the contributions of 'early mass quenching' and mass-independent 'environmental quenching' models in each of these radial regimes. We find the core to be described primarily by early mass quenching, which we interpret as accelerated quenching of massive galaxies in protoclusters, possibly through merger-driven AGN feedback, and the non-core to be described by environmental-quenching, signifying the increase of mass-independent quenching mechanisms that dominate low redshift clusters.

Acknowledgements

I would like to first thank Dr. Michael Balogh for his supervision, advice, patience, and support over these past two years. This project would not have been possible without his guidance, motivation, and willingness to answer my countless questions. I am incredibly fortunate to have had a supervisor who has helped me learn and grow as much as I have throughout this degree.

I would also like to thank my Mom and Dad and the rest of my family for the never ending love and support, as well as my calls and impromptu trips home. I would like to thank Jordan and Kat and all the members of the WCA who have helped and mentored me. I could not have done this without you all.

Finally I would like to thank Amy. For always being there after my late nights at the office, for always listening to me as I recount the hurdles of the day, and for always knowing the perfect thing to say to keep me going.

Dedication

To Grandma and Grandpa, for always making me excited to share what I've been up to. I hope I've made you both proud.

Table of Contents

Author's Declaration ii

Statement of Contributions iii

Abstract iv

Acknowledgements v

Dedication vi

List of Figures ix

List of Tables xv

1 Introduction 1

2 Data 9

2.1 GOGREEN and GCLASS 9

2.2 Galaxy Classification 10

2.3 Sample Weights 11

2.3.1 Membership Correction Factor 11

2.3.2 Completeness Weight 16

2.3.3 Total Weight 16

2.4 The addition of SpARCS-1033 17

3 Methods **24**
3.1 Extension of the Schechter Function . . . 24
3.2 Likelihood Function . . . 25
3.2.1 Stellar mass dependence, $\mathcal{L}_{M,i,x}$ . . . 25
3.2.2 Radial dependence, $\mathcal{L}_{R,i,x}$ . . . 26
3.2.3 Combined Likelihood . . . 28
3.2.4 Weight incorporation . . . 29
3.3 Model Validation . . . 29

4 Results **32**
4.1 Radial Profiles and Quenched Fraction . . . 33
4.2 Stellar Mass Function Fits . . . 43
4.2.1 Star-Forming Population . . . 43
4.2.2 Quiescent Population . . . 44
4.3 Constraining Parameters and ΔBIC . . . 47

5 Discussion **55**
5.1 Literature Comparison . . . 55
5.2 Simple Quenching Pathway Model . . . 57
5.3 Interpretation . . . 62
5.4 Future Work . . . 63

6 Summary and Conclusions **65**

References **67**

APPENDICES **75**

A Redshift Dependence Likelihood **76**

List of Figures

1.1 Figure 3 from Klypin et al. (2016) showing the redshift evolution of halo mass functions in four different simulations all using the cosmological parameters they state in their Table 1. 3

1.2 Figure 2 from Wechsler & Tinker (2018) showing the galaxy stellar-to-halo mass ratio for galaxies at $z = 0$. The figure shows constraints on this relationship based on a number of different measurement methods. The top of the figure shows the halo mass regimes where specific feedback mechanisms are the most effective. The bottom sub-images in the figure show the structure of typical galaxies within the corresponding halo masses. 5

2.1 Rest-frame U-V vs. V-J for all cluster members with $R < R_{200}$ and $M > M_{lim}$ values evaluated with their respective clusters. The black border indicates the distinction between star-forming and quiescent, given in Eq. 2.2. 13

2.2 Distribution of galaxies by the combination of their photometric and spectroscopic differentials, with respect to their cluster center. Green and yellow points are spectroscopic members, and green and red points are photometric members. The galaxies have a cut of $R < R_{200}$ and $M > M_{lim}$ of their respective clusters. 14

2.3 Distribution of galaxies with just photometric measurements (black) and those with spectroscopic values (coloured points), through mass and cluster-centric radius, showing the members and how they contribute to the membership correction factor. 15

2.4 Comparison of R_{200} values calculated using MAMPOSSt, and R_{200} values calculated using Eq. 2.6. The value of A was fit so as to minimize the difference between the two methods of calculation. 19

2.5 Line-of-sight velocity of spectroscopically confirmed cluster members of SpARCS-1033 and non-cluster members with spectra, against their projected cluster-centric radial values. The dashed lines show the velocity dispersion of the cluster. 20

2.6 Recovery rate of injected mock sources against their injected magnitudes. The limiting magnitude is set as the value where the recovery rate is 80% (solid grey line), with the value of 24.15 shown with the dashed grey line. This form is the "naive completeness", without the inclusion of magnitude bias and Eddington bias. 21

2.7 Binned difference between the recovered and injected magnitudes of the injected mock samples against their recovered magnitudes. The fit shows the tendency for `SExtractor` to measure sources as fainter than their true values. 22

2.8 Relation to approximate the mass-to-light ratio for the 11 GOGREEN clusters given in vdB20, plotted against the mean redshift of each cluster. The black dotted fit line allows us to extend the relation to the redshift of SpARCS-1033, and solve for its limiting stellar mass. 23

3.1 Corner plot of parameter recovery from a mock dataset. The figure validates that the parameter recovery of the model, with all the true parameter values within the 1-σ posterior range of the recovered parameter values, as indicated with the red dots at the center of each red cross. This specific fit was run on a set of 10,000 samples for 1500 iterations and 50 walkers. . . . 31

4.1 Complete corner plot of all parameters fit with the sample, corresponding to the values in Table 4.1. The 16, 50, and 84 percentiles (the 1-σ constraints) are shown with the vertical dashed lines in the 1-D histograms. The plot was constructed using the `corner` software (Foreman-Mackey, 2016). . . . 36

4.2 Surface number density of cluster galaxies as a function of cluster-centric radius for the quiescent and star-forming populations, with comparison to fits with the concentration values found in Biviano et al. (2021). 37

4.3 Global quenched fraction dependence on stellar mass, for all radial and redshift values. The errors correspond to the binomial confidence intervals of each binned point. The field value corresponds to the quenched fraction values of field galaxies in the redshift range of the sample, following the fits from McLeod et al. (2021). 38

4.4 Binned points of the sample and the fit form of the quenched fraction as a function of cluster-centric radius. The sample is split into two bins based on the mean redshift of the sample ($z \simeq 1.12$). The high redshift binned points are slightly offset from their original position matching that of the low redshift binned points, for a simplified visual effect. The quenched fraction function (Eq. 3.15) is evaluated at the mean redshift values of each of the bins. The errors on the binned points are their corresponding binomial confidence intervals, and the errors on the fits are the 1-σ parameter errors. The field value is set to the global field quenched fraction value at the mean redshift of the sample following the fit functional form from McLeod et al. (2021). 39

4.5 The fit quenched fraction as a function of redshift, evaluated on the mean cluster velocity dispersion of the sample ($\sigma = 891$ km/s). The errors are the 1-σ parameter errors. The binned points show the quenched fraction of the individual 17 clusters in the sample and their corresponding binomial confidence intervals. The field reference corresponds to the fit quenched fraction function from McLeod et al. (2021). 40

4.6 The modelled quenched fraction as a function of velocity dispersion of the clusters, including the $\pm$1-σ parameter uncertainties. Also shown in the binned quenched fraction of the individual clusters, with their confidence intervals as the vertical errors and their errors in velocity dispersion as their horizontal errors, with the values matching those in Balogh et al. (2021). . 41

4.7 Binned points of the sample and the fit form of the quenched fraction as a function of cluster-centric radius. The sample is split into two velocity dispersion bins based on the mean velocity dispersion of the sample ($\sigma \simeq$ 891 km/s). The function is evaluated at the mean redshift of the cluster ($z \simeq 1.1$), with its errors being the 1-σ parameter uncertainties. The errors on the binned points are their binomial confidence intervals. 42

4.8 Binned number density against stellar mass points for the star-forming galaxy population through two radial bins and three redshift bins. Overlaid is the comparison of the complete model (the blue 'Full Model' fit) evaluated at the mean z and R/R_{200} values of each group (which are stated in each sub-figure), against a non radial or redshift dependent Schechter function fit for just the population in each subgroup (the light blue 'Simple Model' fit). 44

4.9 *Top*: The fit star-forming α parameters as a function of R/R_{200}, with their 1-σ parameter errors. The functions are evaluated for two constant redshifts: $z = 0.95$ (blue) and $z = 1.4$ (red), which are the edges of the range of the entire sample. *Bottom*: The fit star-forming α parameters as a function of z, with their 1-σ parameter errors. The functions are evaluated for two constant radial positions: $R/R_{200} = 0.1$ (yellow) and $R/R_{200} = 0.9$ (green). In both figures, the binned points correspond to the simple model α values and their parameter errors from the six sub-populations in Figure 4.8. In both figures, the values are compared to the star-forming field α values from McLeod et al. (2021). 45

4.10 *Top*: The fit star-forming M^* parameters as a function of R/R_{200}, with their 1-σ parameter errors. The functions are evaluated for two constant redshifts: $z = 0.95$ (blue) and $z = 1.4$ (red), which are the edges of the range of the entire sample. *Bottom*: The fit star-forming M^* parameters as a function of z, with their 1-σ parameter errors. The functions are evaluated for two constant radial positions: $R/R_{200} = 0.1$ (yellow) and $R/R_{200} = 0.9$ (green). In both figures, the binned points correspond to the simple model M^* values and their parameter errors from the six sub-populations in Figure 4.8. In both figures, the values are compared to the star-forming field M^* values from McLeod et al. (2021). 46

4.11 Binned number density against stellar mass points for the quiescent galaxy population through two radial bins and three redshift bins. Overlaid is the comparison of the complete model (the red 'Full Model' fit) evaluated at the mean z and R/R_{200} values of each group (which are stated in each sub-figure), against a non radial or redshift dependent Schechter function fit for just the population in each subgroup (the pink 'Simple Model' fit). 48

4.12 *Top*: The fit quiescent α parameters as a function of R/R_{200}, with their 1-σ parameter errors. The functions are evaluated for two constant redshifts: $z = 0.95$ (blue) and $z = 1.4$ (red), which are the edges of the range of the entire sample. *Bottom*: The fit quiescent α parameters as a function of z, with their 1-σ parameter errors. The functions are evaluated for two constant radial positions: $R/R_{200} = 0.1$ (yellow) and $R/R_{200} = 0.9$ (green). In both figures, the binned points correspond to the simple model α values and their parameter errors from the six sub-populations in Figure 4.11. In both figures, the values are compared to the quiescent field α values from McLeod et al. (2021). 49

4.13 *Top*: The fit quiescent M^* parameters as a function of R/R_{200}, with their 1-σ parameter errors. The functions are evaluated for two constant redshifts: $z = 0.95$ (blue) and $z = 1.4$ (red), which are the edges of the range of the entire sample. *Bottom*: The fit quiescent M^* parameters as a function of z, with their 1-σ parameter errors. The functions are evaluated for two constant radial positions: $R/R_{200} = 0.1$ (yellow) and $R/R_{200} = 0.9$ (green). In both figures, the binned points correspond to the simple model M^* values and their parameter errors from the six sub-populations in Figure 4.11. In both figures, the values are compared to the quiescent field M^* values from McLeod et al. (2021). 50

4.14 The fit quiescent α parameter as a function of R/R_{200} on the model parameter subset where the quiescent α is only allowed to vary with radius. This model configuration corresponds to 'Base + $a_{\alpha,r}$' within Table 4.2. The binned points correspond to individual fit values of four radial sub-populations (with no redshift binning). The field values from McLeod et al. (2021) are also overlaid. 53

4.15 The fit quiescent M^* parameter as a function of R/R_{200} on the model parameter subset where the quiescent M^* is only allowed to vary with radius. This model configuration corresponds to 'Base + $a_{M^*,r}$' within Table 4.2. The binned points correspond to individual fit values of four radial sub-populations (with no redshift binning). The field values from McLeod et al. (2021) are also overlaid. 54

5.1 Adaption of Figure 4 in Papovich et al. (2018), showing the fit of the quiescent α and M^* values for the cluster core and the cluster non-core regions in our sample, compared to the results from ZFOURGE and NMBS in their work through a wide range of redshifts. We utilise the same symbol for our cluster non-core region as their 'highest density quartile' to emphasize the similarity of the environment of these two regimes. The grey shaded regions represent the mean range of parameter values for the 'lowest density quartile' environments. 57

5.2 The combined total SMFs of the cluster core (brown) and the cluster outskirts (green) with their respective $\pm$1-σ errors. Also shown is the total field SMF evaluated from the fit parameters from McLeod et al. (2021). The figure highlights the similarity of the cluster non-core region with the field populations, and the significant difference of the cluster core population from them both. 58

5.3 *Top*: Various combinations of the field star-forming and quiescent SMFs (coloured dashed curves) to replicate the form of the cluster core quiescent SMF (solid red curve with $\pm$1-σ errors). *Bottom*: Same as above but with the M^* value of the quiescent field SMF increased by 0.24 dex, to better show the degree of environmental quenching the model can include. The model parameters are constrained to match the normalization of the quiescent cluster population within our stellar mass range ($M_* > 10^{9.5} M_\odot$). . . . 60

5.4 Various combinations of the field star-forming and quiescent SMFs (coloured dashed curves) to replicate the form of the cluster non-core quiescent SMF (solid red curve with $\pm$1-σ errors). The model parameters are constrained to match the normalization of the quiescent cluster population within our stellar mass range ($M_* > 10^{9.5} M_\odot$). 61

List of Tables

2.1 A comparison of the average depths (taken as the 5-σ limits) of all the GOGREEN clusters and the 1-σ spread between them. Below is comparing the similar 5-σ depths of comparable stacks in the COSMOS/UltraVISTA catalogues (vdB20). 10

2.2 An overview of the 17 GOGREEN and GCLASS clusters and their properties. $^{(a)}$Clusters with offset BCGs, overridden with positions given in van der Burg et al. (2013). $^{(b)}$The stellar mass limits of the quiescent population of each cluster. For the star-forming population, the limit extends down by 0.2 dex due to their smaller mass to light ratio, in accordance with vdB20. 12

4.1 An overview of the 21 parameters, the prior ranges they were evaluated on, and their best-fit posterior values with their 1-σ/68% confidence limits. The prior ranges all correspond to flat priors. $^{(a)}$The upper range of the prior for $f_{q,\circ}$ is set so the overall f_q term is less than 1. 35

4.2 Select combinations of model parameter subsets, along with their BIC value and their ΔBIC value relative to the 'Base' combination (given in § 4.3). . 52

Chapter 1

Introduction

The current model that best describes the initial conditions through to the present large-scale structure of the Universe, is the flat ΛCDM model. The model describes a universe that begins in a hot, dense initial state, and how its components interact with and drive the evolution and expansion. The model expresses the universe as comprised of three components: radiation, matter, and dark energy (Planck Collaboration et al., 2020). Dark energy is a hypothetical form of energy proposed to explain the cosmological constant which describes the late-time accelerated expansion of the Universe (Carroll et al., 1992; Carroll, 2001). It is described as a homogeneous energy with a negative pressure, that retains constant density through the expansion of space (Padmanabhan, 2003; Peebles & Ratra, 2003). The matter component is composed of ordinary baryonic matter ($\sim 16\%$), but is predominantly composed of dark matter ($\sim 84\%$), which is necessary to explain the motion of luminous matter within individual galaxies and clusters (Zwicky, 1933, 1937; Einasto et al., 1974; Ostriker et al., 1974). The dark matter component is described as *cold dark matter* (CDM), or non-relativistic, which allows it to gravitationally collapse early in the Universe's history before the decoupling of baryonic matter from the radiation field, allowing for increased growth of structure (Blumenthal et al., 1984). We are able to understand the initial density conditions of all matter from the act of decoupling, as the photons can propagate out from the 'time of last scattering' unperturbed. The photons that are detected now have been redshifted to peak in the microwave regime, giving rise to the Cosmic Microwave Background (CMB) (Penzias & Wilson, 1965).

These initial density fluctuations also seed the growth of the Universe's structure, with these tiny differences in density increasing due to gravitational instability (Jeans, 1902; Gamow & Teller, 1939; Peebles, 1965; Zeldovich, 1972). Through the buildup of various growth and collapse models (e.g. Zel'dovich, 1970; Gunn & Gott, 1972), the eventual

Press-Schechter theory allowed for the estimation of the mass function of collapsed dark matter halos (Press & Schechter, 1974). This builds on the idea of hierarchical clustering of structure proposed by Peebles (1965), which is possible if the initial density fluctuations survive on small-scales (as is the case in the CDM model), allowing structure to form in a 'bottom-up' manner. There has been a large amount of simulation work done to study and model how these halo mass functions alter with redshift and different cosmologies (such as Jenkins et al., 2001; Springel, 2005; Tinker et al., 2008; Klypin et al., 2016; Bocquet et al., 2020; Seppi et al., 2021). Figure 1.1 shows the redshift evolution of simulated halo mass functions from $0 < z < 5.5$ for a variety of simulations using the Planck cosmological parameters. This figure illustrates the hierarchical assembly of halos, with the amount of massive halos increasing progressively with time.

It is within these dark matter halos that the formation of galaxies occurs, first proposed by White & Rees (1978). Baryonic matter falls into the deep potential wells of the halos, and with the increased proximity of the particles, cooling mechanisms such as bremmstrahlung emission, collisional excitation, and recombination all become more efficient. This results in the gas condensing further under its own gravity, where at the center of the halo the formation of stars and galaxies can occur. However, the use of this simple cooling and collapse model in early simulations would typically result in a runaway effect that led to an overproduction of massive galaxies and unrealistic luminosity functions (Cole, 1991). This was deemed the 'overcooling problem', and can be solved by the inclusion of feedback, with the newly formed stars halting further formation by heating the surrounding gas through stellar winds and supernovae explosions (White & Frenk, 1991). For galaxies in low mass halos, this mechanism can have a global effect, shutting down star formation entirely (Dekel & Silk, 1986; Hopkins et al., 2012). For high mass halos, the energy released from the infall of matter onto a galaxy's supermassive black hole, known as active galactic nucleus (AGN) feedback, becomes the dominant feedback mechanism (Silk & Rees, 1998; Croton et al., 2006). Figure 1.2 shows the galaxy stellar-to-halo mass ratio, which helps visualize the effect that both of these feedback mechanisms have on suppressing star formation within galaxies.

The formation of stars within galaxies is not solely affected by internal feedback processes, but is also impacted by the host galaxy's local environment. By using wide-field surveys and by mapping the spatial distributions of galaxies within them, it is possible to show how these environments fit into the large-scale structure of the Universe. Nearby galaxies often cluster together to create galaxy groups, and these can further cluster together to create high-density galaxy clusters. Clusters often act as nodal points, connecting lower-density structures such a filaments and sheets that flow into higher density areas (Zel'dovich, 1970; Brinckmann et al., 2016). This flow of matter results in the formation

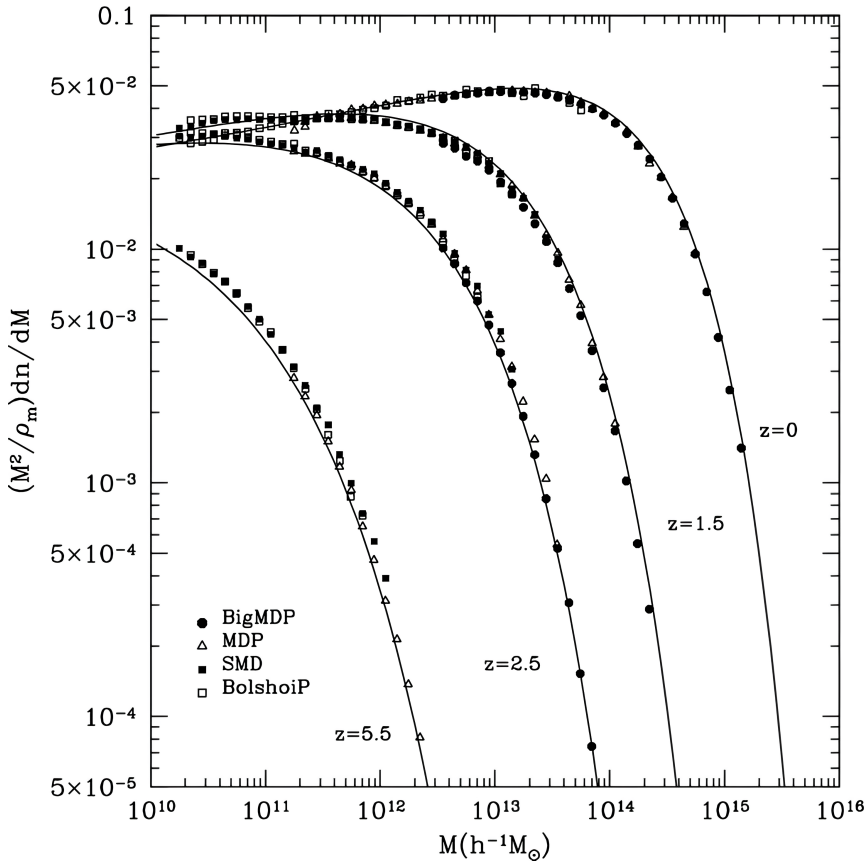


Figure 1.1: Figure 3 from Klypin et al. (2016) showing the redshift evolution of halo mass functions in four different simulations all using the cosmological parameters they state in their Table 1.

and expansion of extremely low density regions called voids (Cautun et al., 2014). Together, the combination of all these interconnected structures (clusters, filaments, sheets, and voids) create the 'cosmic web' of the Universe (Bond et al., 1996).

The term used for the global suppression and rapid cessation of star formation in a galaxy is *quenching*. It describes the process of transitioning a 'blue' star-forming galaxy to a 'red' passive one. This bimodality of cluster type is seen consistently at all redshifts and with no major population present within the transitionary 'green valley', which indicates that quenching occurs on a fairly rapid timescale (Peng et al., 2010; Wetzel et al., 2012). This rapid transition due to quenching is separate yet correlated with the gradual decrease in the average star formation rate (SFR) that is observed, with the peak at $z \approx 2$ (Hopkins & Beacom, 2006; Smit et al., 2012; Madau & Dickinson, 2014; Santini et al., 2017). The relation between the SFR and the stellar mass (the so-called 'star formation main-sequence') shows a tight mass dependency and an increasing normalization with redshift, both of which are attributed to increased rates of gas accretion at earlier times and for more massive halos (Sawicki, 2012; Tomczak et al., 2016; Santini et al., 2017).

A common method of determining the mass distribution of galaxies is through stellar mass functions (SMFs), which show the number density of galaxies as a function of stellar mass. Through observing the evolution of these SMFs, it has been extensively shown that high-mass galaxies were in place at higher redshifts, and that the buildup up of low-mass galaxies occurs through time (Fontana et al., 2006; Rudnick et al., 2009; Ilbert et al., 2013; Muzzin et al., 2013; Tomczak et al., 2014; McLeod et al., 2021; Weaver et al., 2023). This phenomenon, known as 'downsizing' (Cowie et al., 1996), is an anti-hierarchical formation method that is distinct from the hierarchical growth of the dark matter halos they encompass.

The measurement of SMFs by galaxy type (star-forming and quiescent) also gives insight to the formation of quenched galaxies. There is a strong dependency of galaxy type with stellar mass, with massive galaxies dominated by quiescent populations at low redshifts (Kauffmann et al., 2003; Baldry et al., 2004; Bundy et al., 2006; Ilbert et al., 2010, 2013). The mechanisms driving this transition are attributed to the same feedback mechanisms previously mentioned, with supernovae and stellar winds affecting low-mass galaxies, and AGN feedback affecting the more massive galaxies. This fits well with the downsizing model, where not only are the most massive galaxies the first to form, but they are also the first to cease their star formation, while less massive galaxies continue on a more delayed timeline trajectory. There is also an environmental dependency on galaxy type, attributed to the local density surrounding each galaxy, initially observed by Hubble & Humason (1931) and Dressler (1980) through morphological properties, and later through various observational tracers (Kauffmann et al., 2004; Balogh et al., 2004a,b; Baldry et al.,

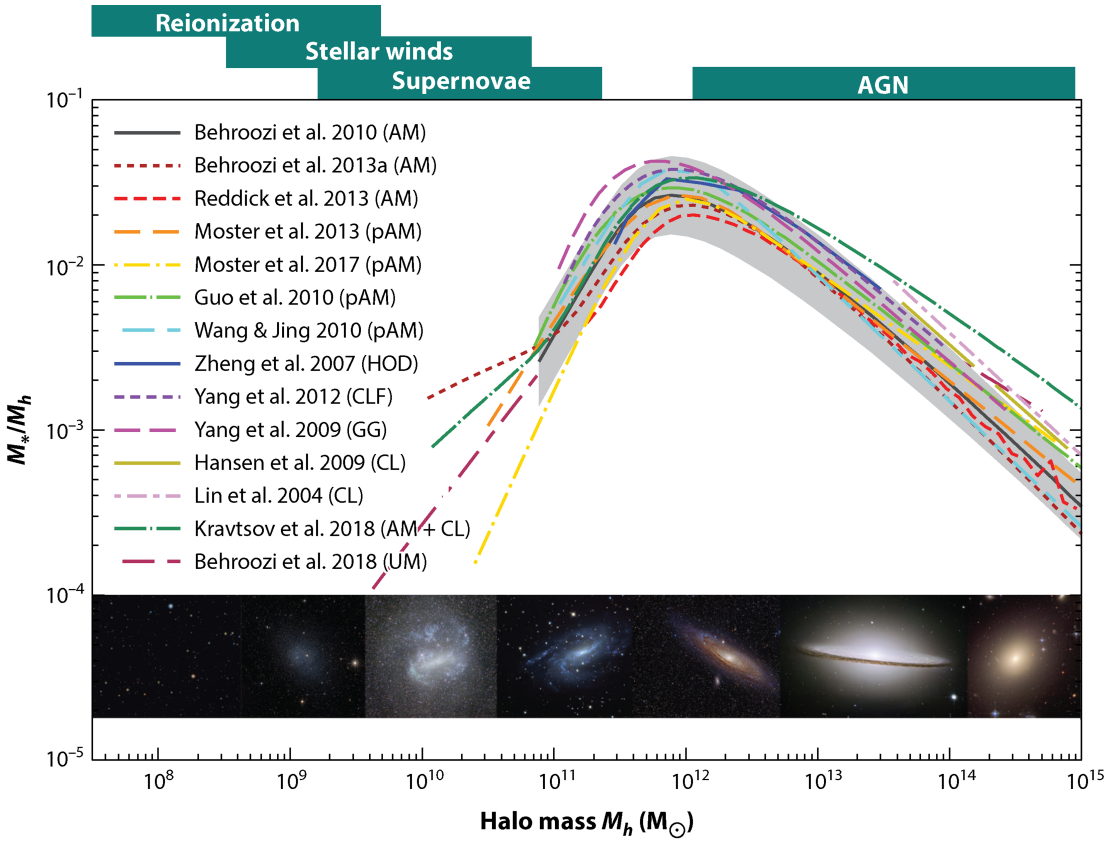


Figure 1.2: Figure 2 from Wechsler & Tinker (2018) showing the galaxy stellar-to-halo mass ratio for galaxies at $z = 0$. The figure shows constraints on this relationship based on a number of different measurement methods. The top of the figure shows the halo mass regimes where specific feedback mechanisms are the most effective. The bottom sub-images in the figure show the structure of typical galaxies within the corresponding halo masses.

2006). This increase in the quenched fraction as a function of density can be seen smoothly through the full range of large scale structures (Gavazzi et al., 2010; Mahajan et al., 2010; Cybulski et al., 2014).

The mechanisms for environmental quenching, which are all externally based and have to do with a galaxy's interaction with its surroundings, can be classified into four main candidates. The first is ram-pressure stripping, which is a process that occurs within galaxy clusters, where the interstellar gas of an infalling galaxy is stripped away by the cluster's intracluster medium (ICM). This ram pressure, first introduced by Gunn & Gott (1972), is induced parallel and opposite to the velocity vector of the galaxy (as the ICM is relatively stationary compared to the infalling galaxy), and is proportional to $P_r \approx \rho_e v^2$, where ρ_e is the ICM density, and v is the velocity of the galaxy. If the pressure exceeds the restoring force that the galaxy has on its colder gas reservoirs (its interstellar medium (ISM)), then the ISM can be actively removed, rapidly halting the ability for new star formation. The effectiveness of this mechanism should then increase with ICM density and infall velocity, as well as with decreasing galaxy stellar mass, however the magnitude of its effect is still in question (Abadi et al., 1999; Merluzzi et al., 2013; Bekki, 2014; Quilis et al., 2017; Tonnesen, 2019). Another mechanism is starvation or strangulation, which similar to ram-pressure stripping in that it induces quenching through the removal of gas by the ICM. Starvation however does not actively remove gas from the ISM, but instead removes the hot ionized gas in the outer halo of the galaxy (the circumgalactic medium). This halts the replenishment of the HI and eventual cold H_2 gas, thus starvation results in a delayed quenching effect that depends on the gas consumption timescales of the galaxy (Larson et al., 1980; Balogh et al., 2000; Balogh & Morris, 2000; Peng et al., 2015; Maier et al., 2016; Vaughan et al., 2020). The above mechanisms do not primarily transform the stellar morphology of galaxies (Weinmann et al., 2006; van den Bosch et al., 2008; Kawinwanichakij et al., 2017), unlike the final two mechanisms, which are caused by strong gravitational interactions. These mechanisms are galaxy-galaxy mergers, which are the direct collisions of two (or more) galaxies, and galaxy harassment, which is the cumulative effect of tidal forces due to frequent high-speed galaxy encounters. Both of these mechanisms can have drastic effects on the morphology of the interacting galaxies, with harassment quenching through the violent removal of gaseous and stellar material in the form of stellar streams, and with mergers inducing starbursts which decrease the gas depletion timescale, or potentially feeding AGN activity, both of which result in accelerated quenching timelines for the galaxy (Moore et al., 1996; Smith et al., 2010; Bialas et al., 2015; Boselli et al., 2016).

From this it is shown that there are two classifications of quenching processes: mechanisms that are effective due to a galaxy's mass, and mechanisms that are effective due to

a galaxy's environment. The work of Baldry et al. (2006) and Peng et al. (2010) explored the effectiveness of 'mass-quenching' and 'environmental-quenching' processes, and found both to be independent of each other. However, their work focused on the local universe ($z = 0$), and subsequent works have shown that the quenching efficiencies evolve with time, and that this separability does not hold at higher redshifts (Balogh et al., 2016; Kawinwanichakij et al., 2017; Papovich et al., 2018; Pintos-Castro et al., 2019; van der Burg et al., 2020). In particular, the work of Balogh et al. (2016) and van der Burg et al. (2020) (hereafter vdB20) looked at massive galaxy clusters at $0.8 < z < 1.4$ in the GCLASS and GOGREEN surveys, described in § 2.1, with both finding a strong mass dependency for the quenched fraction excess (QFE). This indicates that massive galaxies are preferentially quenched in clusters *in addition to* the mass-dependency of field mass-quenching. This is in direct contradiction of the mass-independent environmental quenching model proposed in Peng et al. (2010). Furthermore, although an elevated quenched fraction was found in the clusters, the individual star-forming and quiescent SMFs in vdB20 had exactly the same shape as their equivalent field galaxies. In the Peng et al. (2010) model, the excess of environmentally quenched galaxies are assumed to be built up in a mass-independent manner, which requires the quiescent cluster and field galaxies to have different SMF shapes, notably with an increase of the low-mass slope in the cluster SMF. However, no signature of this was found, suggesting an alternative environmental quenching mechanism in high redshift clusters that mimics the mass dependency of mass-quenching.

These massive galaxies in the GOGREEN sample were explored further in Webb et al. (2020), who found them to be older than the field galaxies. However, their models showed that pre-processing (the initiation of environmental quenching when galaxies become satellites but before cluster infall) was still required to achieve the observed quenched fraction. Additional works further validated the need for the pre-processing, with almost all massive galaxies found to be quenched prior to cluster infall (McNab et al., 2021; Reeves et al., 2021; Werner et al., 2022). The work of McNab et al. (2021) found the low-mass cluster galaxies to have elevated fractions of post-starbursts and green valley galaxies (galaxies that have recently quenched, and galaxies currently undergoing quenching, respectively), and Werner et al. (2022) found that a constant $\sim 40\%$ of all star-forming low-mass galaxies quench after infall. These indicate that the environmental-quenching of low-mass galaxies is more similar to the mass-independent Peng et al. (2010) model, without the need for pre-processing. This suggests there are multiple potential processes to build up the observed cluster populations. Alternatively however, work from Baxter et al. (2022) showed that the observed mass-dependency of the cluster environmental-quenching could be reproduced using a quenching time-scale model that was also mass-dependent, allowing for starvation to be the dominant cluster quenching mechanism. They built upon this in Bax-

ter et al. (2023) where they explored the radial dependence of the quenching timescale, and ruled out ram-pressure stripping to be the mechanism that creates the elevated quenched fraction in the cluster core.

With the culmination of these results it is evident that further analysis of these clusters is necessary to constrain the distinct quenching processes that are in place at these high redshift clusters. To do so we explore in this work how the mass dependency of environmental effects change within the cluster and evolve with time. This is done by fitting SMFs to the full sample of the GOGREEN and GCLASS clusters, and letting the shape parameters of each population (star-forming and quiescent) vary with cluster-centric radius and redshift. With indication of further dependencies from previous literature results, we also constrain the radial profiles of the red and blue galaxies to find the quenched fraction, and fit parameters that describe how it varies as a function of redshift and cluster velocity dispersion.

The remainder of this thesis is structured as follows: in Chapter 2 we discuss the cluster sample with galaxy type and membership classification, along with the cluster completeness and the associated weights on the data. Chapter 3 discusses the methodology for constructing the likelihood function and the extension of the base Schechter function, as well as the model validation techniques. In Chapter 4 we present our results for the model fit, and additional constraints on the model to find the most significant parameters. In Chapter 5 we discuss these results, comparing them to previous literature and how this impacts our understanding of quenching in clusters. We also explore simple toy models that constrain the general quenching processes within the sample. Chapter 6 then summarises the thesis and conclusions found in this work.

In this work we adopt the ΛCDM cosmology parameters with $\Omega_m = 0.3$, $\Omega_\Lambda = 0.7$, and $H_0 = 70$ km s^{-1} Mpc^{-1}. All magnitudes stated are in the absolute bolometric (AB) magnitude system. Any uncertainties presented are given at the 1-σ level, unless otherwise stated.

Chapter 2

Data

2.1 GOGREEN and GCLASS

The data used in this study comes from two surveys, the Gemini Observations of Galaxies in Rich Early ENvironments (GOGREEN) survey (Balogh et al., 2017) and the Gemini CLuster Astrophysics Spectroscopic Survey (GCLASS) (Muzzin et al., 2012). Together, the surveys observed 26 overdense systems (a combination of seventeen massive galaxy clusters and nine groups), spanning a range of $0.87 < z < 1.46$ (Balogh et al., 2021). Fourteen of the clusters were drawn from the *Spitzer* Adaptation of the Red Cluster Sequence (SpARCS) survey, and the three other clusters were drawn from the South Pole Telescope (SPT) survey.

The aim of GOGREEN and GCLASS was to follow-up on these clusters with deep, multiwavelength photometry using a variety of instruments, as well as substantial multi-object spectroscopy using the GMOS spectrographs. The majority of the clusters have imaging through the *ugriz* bands, the J and K bands, and with all the IRAC channels, and at depths that are comparable to COSMOS/UltraVISTA. Table 2.1 shows this comparison with the average depth of the GOGREEN clusters in some select bands. The photometric redshifts were fit using the `EAZY` code, and when validating those values using galaxies which also had spectroscopic redshifts, they found the sample had 4.1% outside their 'outlier' limit of $|\Delta z| > 0.15$, a mean Δz of 0 (they had implemented a bias correction) and with a scatter around that bias of $\sigma_z = 0.048$ (vdB20). The high completeness of spectroscopic measurements of the samples ($\sim 40\%$) allowed this project to calibrate the photometric redshift-based membership (see § 2.3.1), thus providing an accurate, statistical membership correction to apply to the photometric sample.

Catalogue	***u/U***	***V***	***z/Z***	***J***	K_s	**[3.6]μm**
GOGREEN	26.0±0.3	25.6±0.3	24.9±0.6	24.3±0.3	23.9±0.2	23.5±0.7
COSMOS/UltraVISTA	26.8	26.4	25.2	24.3	23.8	23.9

Table 2.1: A comparison of the average depths (taken as the 5-σ limits) of all the GOGREEN clusters and the 1-σ spread between them. Below is comparing the similar 5-σ depths of comparable stacks in the COSMOS/UltraVISTA catalogues (vdB20).

2.2 Galaxy Classification

The data catalogues were taken from the second Public Data Release (DR2) (Balogh et al., 2021). Only galaxies designated to the twelve GOGREEN and the five GCLASS clusters were considered, disregarding the nine galaxy groups in the catalogues. By taking that subset and removing stellar objects (those with the `Star` flag set to one), the number of objects in the sample drops from the initial 282,855 to 57,528.

The cluster centre is defined as the location of the brightest cluster galaxy (BCG) of each cluster. There are two exceptions to this, SpARCS-1047 and SpARCS-1051, which have BGCs that are strongly offset from a more physical centre, and so their centres are overridden, matching the positions given in van der Burg et al. (2013).

Cluster membership is initially determined by a redshift differential with the cluster centre. The redshift differentials are calculated using their spectroscopic redshift if available, and their photometric redshift if not, using the form:

$$\Delta z_i = \frac{z_i - z_{clust}}{1 + z_i} \tag{2.1}$$

Spectroscopic cluster members are defined as those having a differential of $|\Delta z_{spec}| \leq 0.02$, and photometric cluster members are defined as those having a differential of $|\Delta z_{phot}| \leq 0.08$. These spectroscopic ranges includes galaxies within 2-3 times the typical cluster velocity dispersion ($\simeq$2400-3400 km/s in the rest-frame of the clusters). These differentials are used later on to quantify a membership correction factor. Applying the redshift differential cuts to the data reduces the sample to 10,348.

We also make a spatial cut based on the projected radial distance of the galaxy from their cluster's BCG. The limiting distance is the virial radius of the cluster, R_{200}. The R_{200} values for 14 of the clusters were taken from Biviano et al. (2021), and the values for SpARCS-0219 and SpARCS-1034 were taken from McNab et al. (2021), as those two were

not considered in the former paper due to low numbers of spectroscopic members. The values from Biviano et al. (2021) were calculated using the MAMPOSSt method (described in detail in their work). Due to small sample sizes for the clusters, the only free parameter they fit for was R_{200}, and they use a Burkert profile (Burkert, 1995) for the cluster mass profile $M(r)$, and an Opposite profile (Biviano et al., 2013) for the velocity anisotropy profile $\beta(r)$. The value for SpARCS-1033 was calculated in this work and is discussed in § 2.4. Applying a cut of $R < R_{200}$ reduces the sample to 2780.

To differentiate the galaxies into their star-forming and quiescent distinctions, we utilize the vdB20 criteria, which makes a split in the population based on the distribution of the rest-frame UVJ colours. Quiescent galaxies are defined as the following:

$$U - V > 1.3 \cap V - J < 1.6 \cap U - V > 0.60 + (V - J) \tag{2.2}$$

This distinction can be seen within Figure 2.1, where the rest-frame colours are plotted for galaxies with stellar masses of $M > M_{lim}$ (based on limiting K_s magnitudes - see § 2.3.2), and projected distances of $R < R_{200}$ from their cluster centre.

The list of the 17 galaxy clusters and their properties can be found in Table 2.2. Please note the latter values for SpARCS-1033 were calculated in this work, with the methods described in § 2.4.

2.3 Sample Weights

2.3.1 Membership Correction Factor

Since the majority of the sample galaxies only have photometric measurements, we must correct for the effects of interlopers and missing members. Around 40% of the final sample have spectroscopic redshifts, and by following the same procedure given in vdB20, we break up the population into four distinct groups based on the combination of their spectroscopic and photometric membership status ($|\Delta z_{spec}| \leq 0.02$ and $|\Delta z_{phot}| \leq 0.08$, respectively). Those in agreement of membership status are designated either "secure member" or "secure interloper", while those in disagreement are designated "false negative" or "false positive". The distribution of galaxies with spectra and their designations can be seen in Fig 2.2. A membership weight for each photometric member is created by evaluating the five nearest neighbours in mass and radial space within the correction factor:

$$\text{MCF} = \frac{\mathcal{N}(\text{secure member}) + \mathcal{N}(\text{false negative})}{\mathcal{N}(\text{secure interloper}) + \mathcal{N}(\text{false positive})} \tag{2.3}$$

Cluster Name	$\mathbf{RA}^{BCG}_{J2000}$	$\mathbf{Dec}^{BCG}_{J2000}$	**Redshift**	R_{200} [**Mpc**]	$K_{s,lim}$ [$\mathbf{mag_{AB}}$]	$M_{*,lim}$ [$\log M_\odot$] [(b)]
SpARCS-0034	8.67512	-43.1315	0.867	0.61	21.53	10.42
SpARCS-0035	8.957	-43.206604	1.335	1.01	23.81	9.50
SpARCS-0036	9.18756	-44.1805	0.869	1.21	22.11	10.53
SpARCS-0215	33.84996	-3.72561	1.004	0.89	21.73	10.45
SpARCS-0335	53.7648	-29.48217	1.368	0.76	22.91	10.07
SpARCS-1047[(a)]	161.8893	57.68706	0.956	0.99	22.68	10.17
SpARCS-1051[(a)]	162.79675	58.30075	1.035	0.95	24.17	9.35
SpARCS-1613	243.311	56.825	0.871	1.72	22.55	9.97
SpARCS-1616	244.1722	55.7534	1.156	1.00	23.76	9.59
SpARCS-1634	248.6542	40.3637	1.177	0.88	24.01	9.50
SpARCS-1638	249.7152	40.64525	1.196	0.74	23.94	9.54
SPT-0205	31.451	-58.4803	1.3227	0.80	23.25	9.90
SPT-0546	86.6403	-53.761	1.0669	1.22	23.47	9.64
SPT-2106	316.5191	-58.7411	1.1307	1.24	23.19	9.79
SpARCS-1034	158.706	58.30919	1.385	0.24	24.22	9.55
SpARCS-0219	34.9315	-5.5249	1.325	0.79	23.27	9.90
SpARCS-1033	158.3565	57.89	1.461	1.17	23.89	9.74

Table 2.2: An overview of the 17 GOGREEN and GCLASS clusters and their properties. [(a)]Clusters with offset BCGs, overridden with positions given in van der Burg et al. (2013). [(b)]The stellar mass limits of the quiescent population of each cluster. For the star-forming population, the limit extends down by 0.2 dex due to their smaller mass to light ratio, in accordance with vdB20.

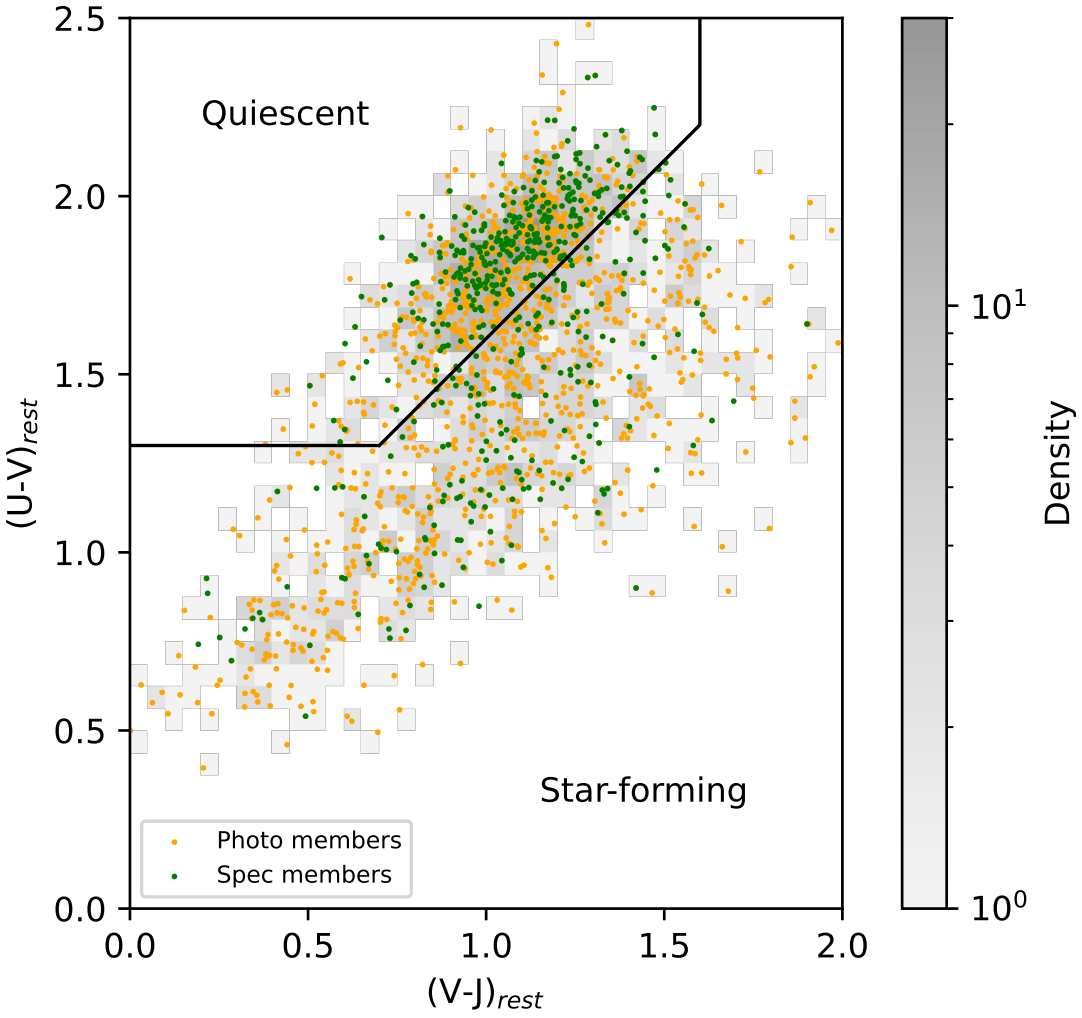


Figure 2.1: Rest-frame U-V vs. V-J for all cluster members with $R < R_{200}$ and $M > M_{lim}$ values evaluated with their respective clusters. The black border indicates the distinction between star-forming and quiescent, given in Eq. 2.2.

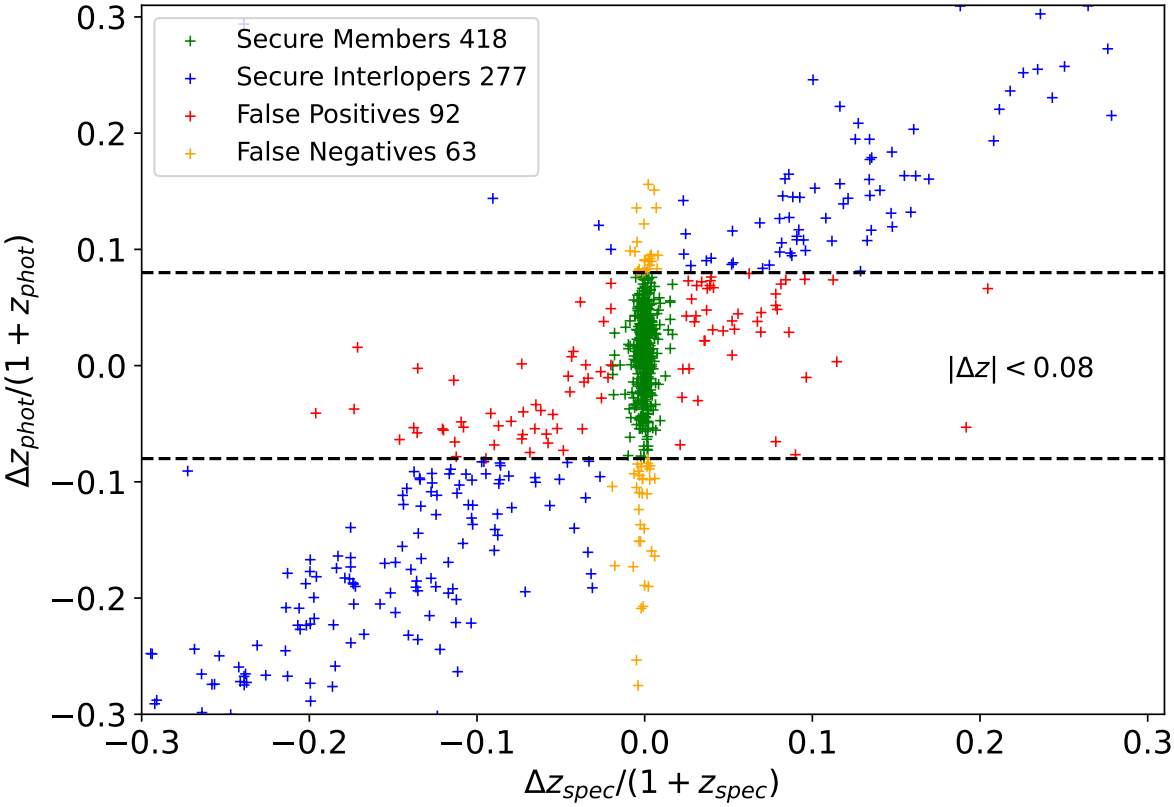


Figure 2.2: Distribution of galaxies by the combination of their photometric and spectroscopic differentials, with respect to their cluster center. Green and yellow points are spectroscopic members, and green and red points are photometric members. The galaxies have a cut of $R < R_{200}$ and $M > M_{lim}$ of their respective clusters.

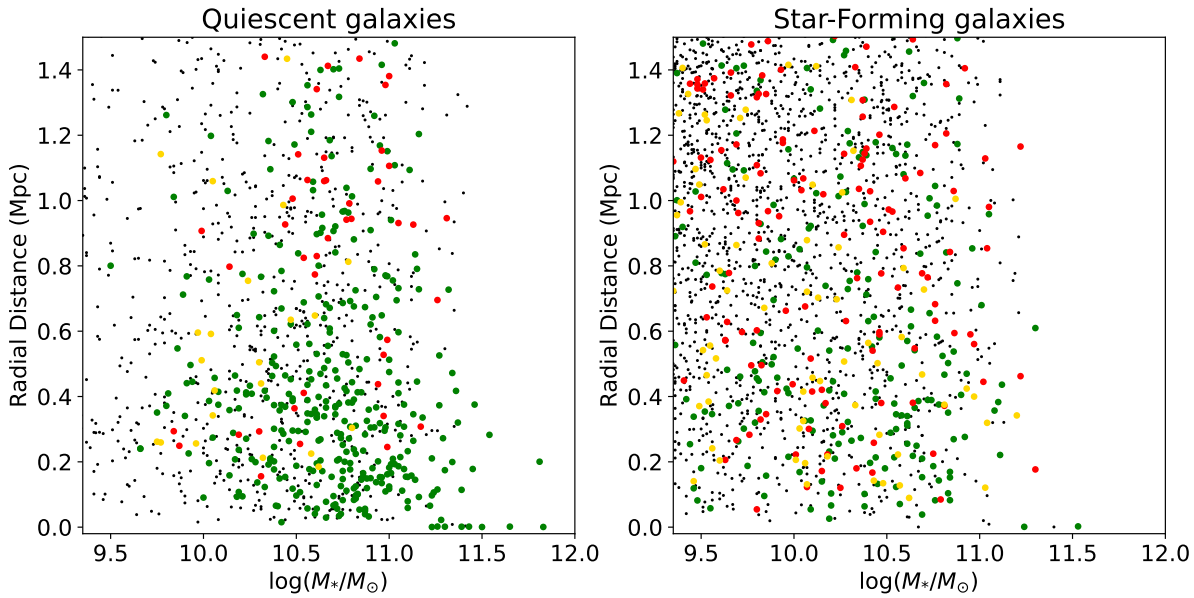


Figure 2.3: Distribution of galaxies with just photometric measurements (black) and those with spectroscopic values (coloured points), through mass and cluster-centric radius, showing the members and how they contribute to the membership correction factor.

where the $\mathcal{N}(X)$ terms are the number of each respective group. This factor allows us to up-weight galaxies that have similar conditions to false negative galaxies, and down-weight galaxies that have similar conditions to false positive galaxies, reducing the influence on our sample from interlopers and making the sample more representative of its true population. The distribution of both photometric and spectroscopic members in stellar mass and projected radial space can be seen in Fig 2.3. It should be noted that galaxies that are spectroscopic members have their membership factor set to 1, regardless of their photometric classification.

2.3.2 Completeness Weight

We include a completeness weight which corrects for incompleteness in the sample, based on the K_s-band measurements of each galaxy. The weight is structured as $1/\mathit{Completeness}(K_s)$, and with the sample constrained to where recovery is >80%, the range of completeness weight values go from 1.0-1.25. The completeness value for a specific galaxy depends on its K_s-band magnitude, and the limiting K_s magnitude ($K_{s,lim}$) of the image of its parent cluster. These limiting magnitude values of each cluster are given in Table 2.2, with the majority of the values, and the associated limiting cluster stellar mass ($M_{*,lim}$), taken from vdB20, excluding the value for SpARCS-1033, which we calculate using the same procedure they describe (see § 2.4).

2.3.3 Total Weight

The overall weight applied to each galaxy is the product of the membership correction factor and the completeness weight, shown in this relation:

$$w_i = \mathrm{MCF}_i \times \frac{1}{\mathrm{Compl}(K_{s,i})} \tag{2.4}$$

This is the weight structure used in the unbinned model fits. However, when comparing the SMF fits with the binned data it is necessary to address the inconsistency of limiting cluster stellar mass across the sample clusters (see Column 7 in Table 2.2), and correct the mass bins that are not equally represented by all clusters. We apply a correction weight to galaxies in these bins which upweights them by the degree of their cluster completeness compared to the rest of the sample, with the increase determined by the various richness values of the sample clusters. We follow the definition of the richness parameter λ in vdB20, which is defined as the number of member galaxies in each cluster (regardless of

galaxy type), with a stellar mass of $M \geq 10^{10.2} M_{\odot}$, and residing within a projected radius of $R \leq 1$ Mpc. The overall cluster completeness weight for a specific cluster is the sum of all richness parameters over the sum of richness parameters of clusters that have mass limits smaller than the stellar mass of the specific galaxy we are evaluating it for. With this weight applied the relation becomes:

$$w_i = \mathrm{MCF}_i \times \frac{1}{\mathrm{Compl}(K_{s,i})} \times \frac{\Sigma_{cl} \lambda_{cl}}{\Sigma_{cl, M_{*,i} > M_{*,lim,cl}} \lambda_{cl}} \tag{2.5}$$

It should be noted that while the richness parameters are independent of galaxy type, the stellar mass limit of a cluster does depend on galaxy type, meaning a star-forming and a quiescent galaxy with the same stellar mass, magnitude, and membership, could have slightly different overall weights.

With these weights we can make some final cuts to the sample. By setting a cut for all galaxy stellar masses to be greater than their limiting cluster stellar mass ($M_{*,i} > M_{lim,cl}$), the sample reduces to 1664, and by making an overall cut of $\log M_* > 9.5$ to match the range of vdB20, the sample reduces to 1620. Finally, by only keeping galaxies with a K_s magnitude larger than the limiting magnitude of their cluster (i.e. $1/\mathrm{Compl}(K_s) < 1.25$), the sample reduces to a final size of 1606, with 833 designated as star-forming and 773 designated as quiescent.

2.4 The addition of SpARCS-1033

In the majority of the previous papers using GOGREEN data, there has been decreased detail or complete omission of one of the clusters: SpARCS-1033 (Balogh et al., 2021; van der Burg et al., 2020; Biviano et al., 2021; McNab et al., 2021). This was due to the lack of equivalent depth of multi-band photometry, and specifically the K-band image, which serves as the detection image for the whole sample. It has since completed the necessary imaging and now can be utilised in the sample. This cluster is important due to it being the highest redshift in the sample ($z = 1.46$), and will help constrain the redshift evolution of the mass functions. In this section we describe the methods to get the values of the cluster characteristics that we describe above for the other clusters.

The work done in Biviano et al. (2021) used the MAMPOSSt method to fit for the R_{200} values of each cluster. Since there are few spectroscopic members for SpARCS-1033, using the full dynamical analysis in Biviano et al. (2021) is not well-justified. Instead we adopt

a similar approach of basing the R_{200} value for SpARCS-1033 on the relation

$$R_{200} = \sqrt{\frac{A}{100}} \frac{\sigma_{LOS}}{H(z)} \tag{2.6}$$

where σ_{LOS} is the line-of-sight velocity dispersion. The value of A was fit for agreement with the values from Biviano et al. (2021) (resulting in a final functional form matching that in Vulcani et al. (2012)), as seen in Fig 2.4.

The line-of-sight velocity dispersion of SpARCS-1033 was calculated using the standard deviation of eight spectroscopic cluster members, defined as being within 1 Mpc and having a redshift differential with the cluster center of less than 0.02. The distribution of cluster members and non-members in radial and velocity space can be seen in Figure 2.5.

Like the other clusters, the limiting magnitude of SpARCS-1033 is based on the recovery rate of mock sources that are injected on the raw K_s-band image. We created the mock sources using the `GALSIM` software (Rowe et al., 2015), and followed the same procedure as vdB20, with all of them being described with the same Sérsic = 1 light profile. The rest of the parameters are randomly drawn from uniform distributions, with the magnitudes in the range of 15-28, the half-light radii in the range of 1-3 kpc, the ellipticities in the range of 0.0-0.2, and all of random orientation. A total of 30,000 mock sources were injected across 60 sets of the raw image, so not to alter the underlying characteristics of the original image. The sources are recovered using `SExtractor` (Bertin & Arnouts, 1996), and the individual recoveries of each run are stacked to give the overall completeness curve, as seen in Figure 2.6.

Following the definition in vdB20, the limiting magnitude is set where the mock source recovery rate is 80%. For the curve shown in Figure 2.6, this corresponds to a magnitude of 24.15 $\mathrm{mag_{AB}}$. However, as noted, the curve shows the recovery of intrinsic magnitudes, and so is missing two main sources of bias. The first is a magnitude bias, which corrects for the discrepancy between the recovered and intrinsic magnitudes of the mock sources, with the binned points and fit shown in Figure 2.7. The second is Eddington bias, which affects the completeness distribution, especially the steep slope at higher magnitudes, with the random magnitude scatter resulting in more brighter sources scattering into the bins of fainter sources (Eddington, 1913). The correction factors for both biases were matched with those in vdB20, leading to a minor correction and giving a limiting magnitude value of 23.89 $\mathrm{mag_{AB}}$ for SpARCS-1033.

With the corrected magnitude limit we are able to calculate the stellar mass limit of the cluster. Given the small range of redshift and limiting masses of the cluster sample, we can estimate the mass limit of SpARCS-1033 via a simple extrapolation of the full

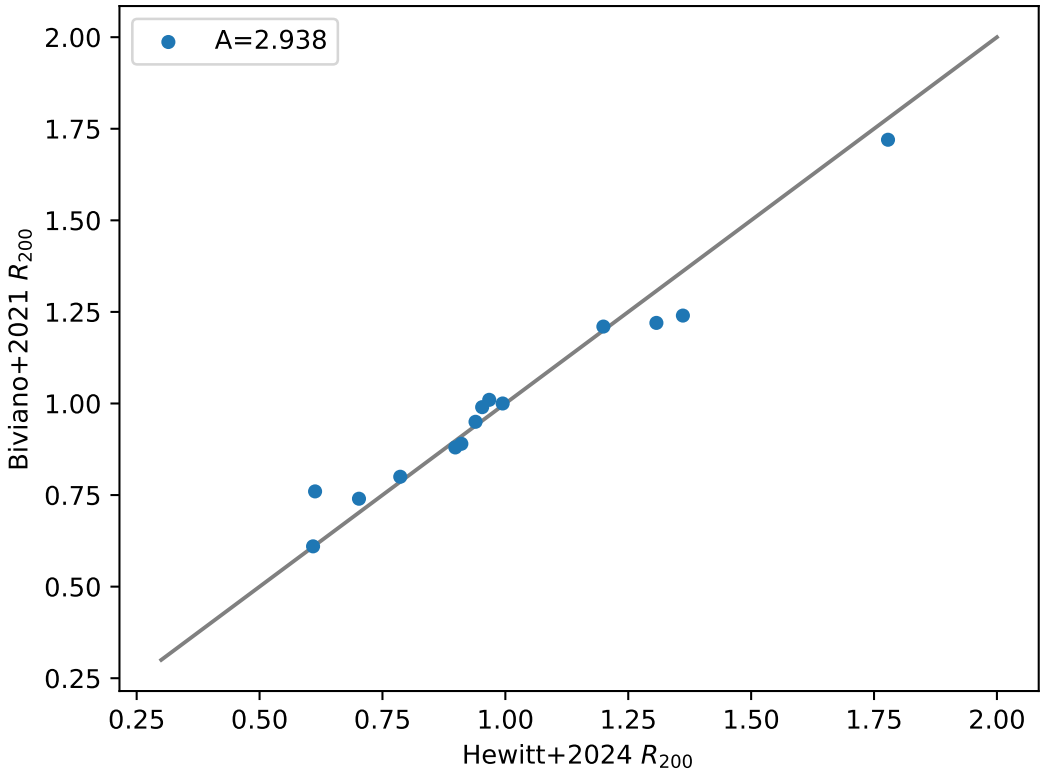


Figure 2.4: Comparison of R_{200} values calculated using MAMPOSSt, and R_{200} values calculated using Eq. 2.6. The value of A was fit so as to minimize the difference between the two methods of calculation.

FAST-derived fits completed for the other clusters in vdB20. Using the stellar mass and magnitude limits, we can solve for the mass-to-light ratios (M_*/L) of each cluster using the relation $\log M_{lim} + 0.4K_{s,lim} = \log\left(\frac{M_*}{L}\right)$. By plotting this relation for each GOGREEN cluster through their redshift, as shown in Figure 2.8, we are able to fit this trend and extend to the redshift of SpARCS-1033 and solve for its limiting stellar mass (stated in Table 2.2).

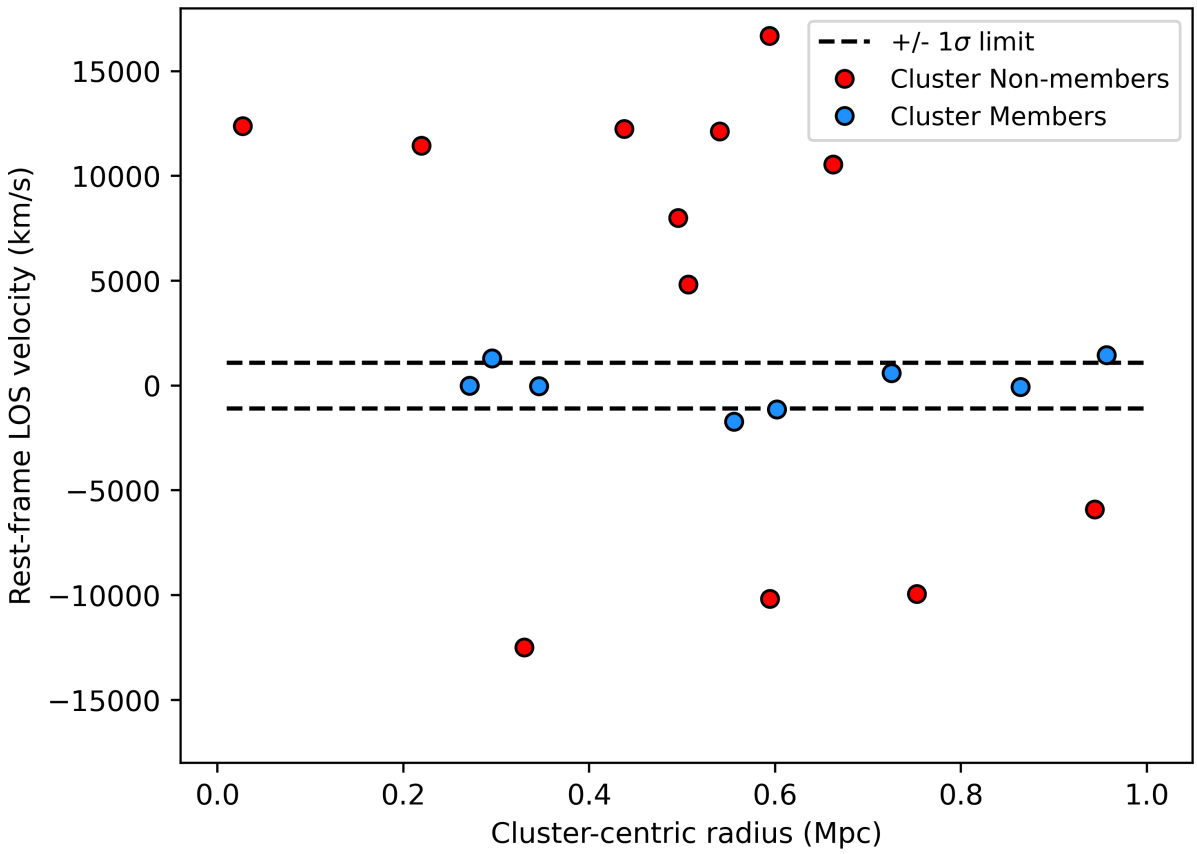


Figure 2.5: Line-of-sight velocity of spectroscopically confirmed cluster members of SpARCS-1033 and non-cluster members with spectra, against their projected cluster-centric radial values. The dashed lines show the velocity dispersion of the cluster.

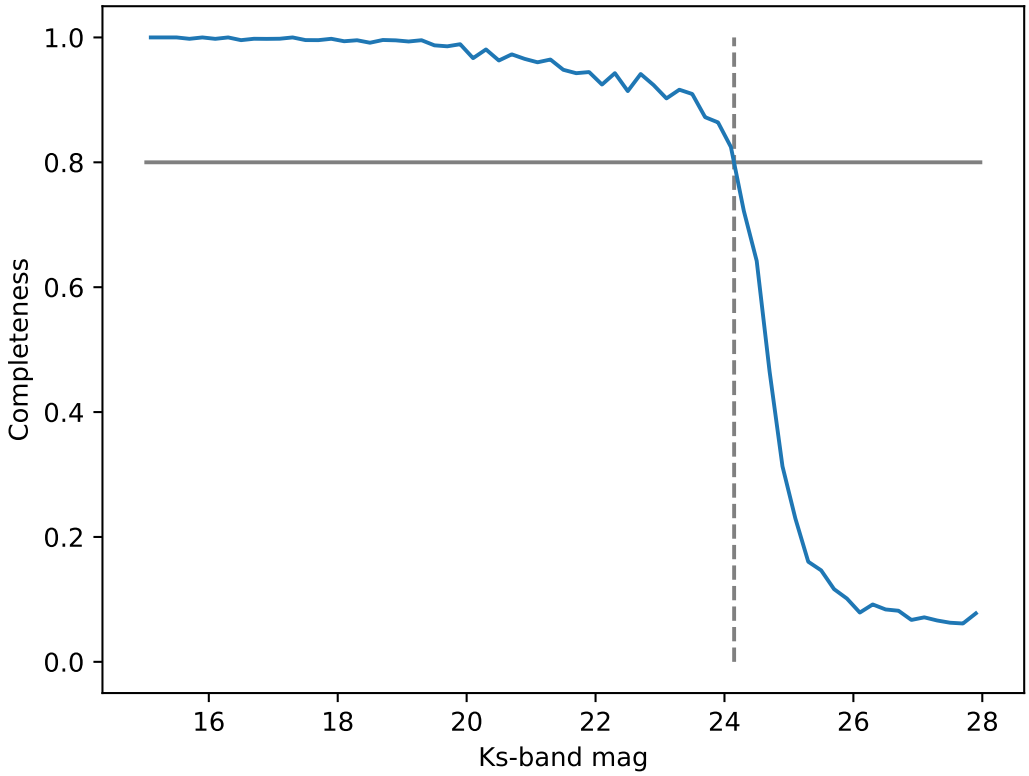


Figure 2.6: Recovery rate of injected mock sources against their injected magnitudes. The limiting magnitude is set as the value where the recovery rate is 80% (solid grey line), with the value of 24.15 shown with the dashed grey line. This form is the "naive completeness", without the inclusion of magnitude bias and Eddington bias.

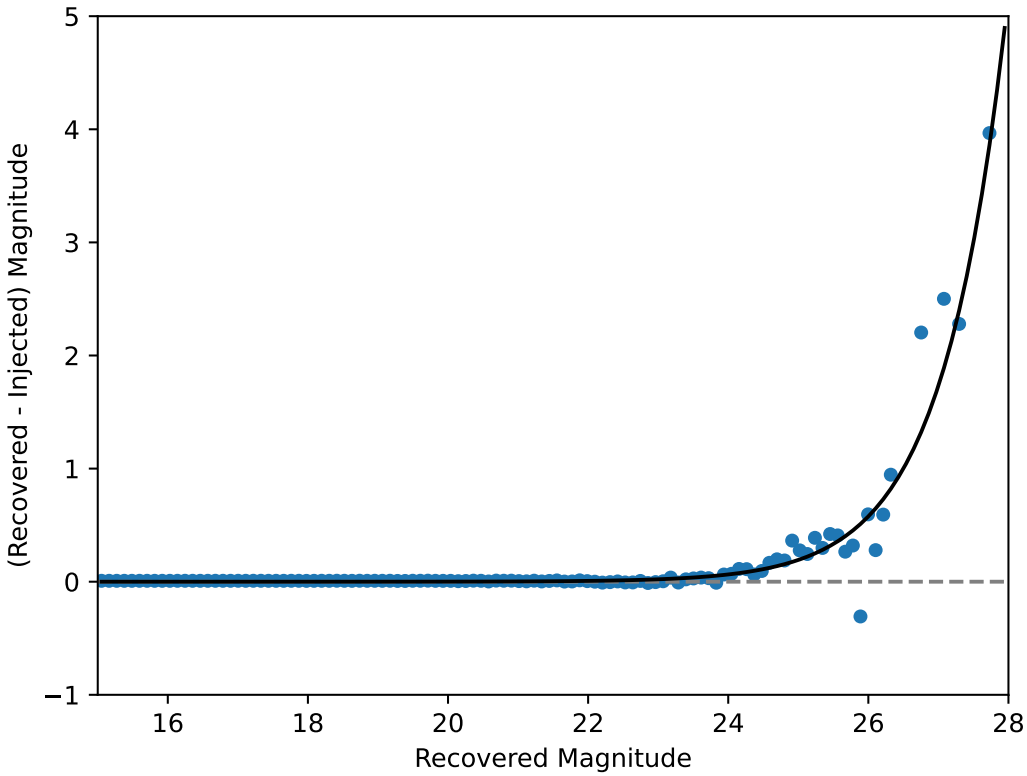


Figure 2.7: Binned difference between the recovered and injected magnitudes of the injected mock samples against their recovered magnitudes. The fit shows the tendency for `SExtractor` to measure sources as fainter than their true values.

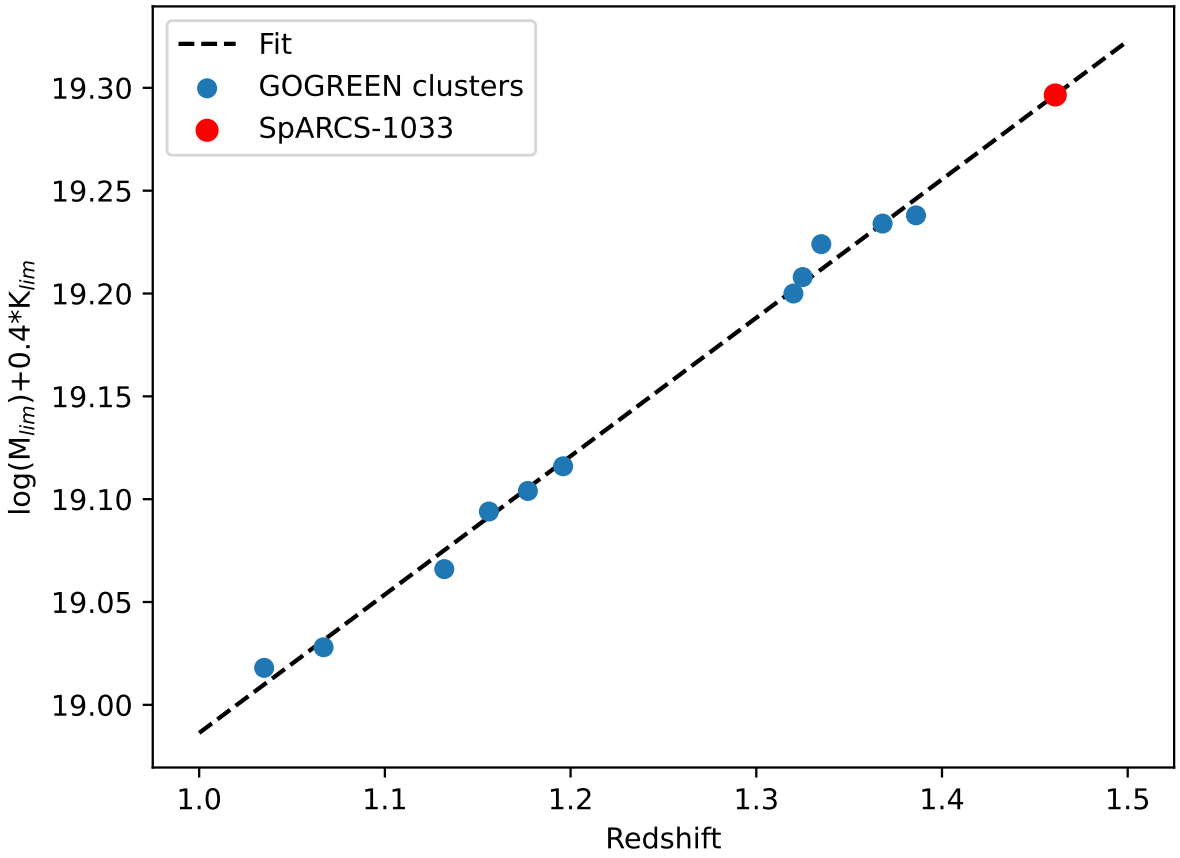


Figure 2.8: Relation to approximate the mass-to-light ratio for the 11 GOGREEN clusters given in vdB20, plotted against the mean redshift of each cluster. The black dotted fit line allows us to extend the relation to the redshift of SpARCS-1033, and solve for its limiting stellar mass.

Chapter 3

Methods

This project aims to use the observations discussed in the previous chapter to describe the shape change of cluster galaxy stellar mass functions through a variety of variables. We do this by modelling how the galaxy populations are altered as a function of their primary characteristics, which in this work we denote as their stellar mass, their cluster-centric radius, and their redshift. This chapter discusses our application of this through the extension of the base Schechter function parameters, so that they are themselves functions of radius and redshift, in addition to the use of radial profiles to constrain the quenched fraction parameters and evolution.

3.1 Extension of the Schechter Function

We model the stellar mass functions (the galaxy number density per stellar mass interval) with a single Schechter function (Schechter, 1976) of the form:

$$\phi(M)dM = \frac{dN}{dM}dM = \phi^* \left(\frac{M}{M^*}\right)^{\alpha} \exp\left(-\frac{M}{M^*}\right) \frac{dM}{M^*}. \tag{3.1}$$

It should be noted that other works consider the number density per logarithmic mass interval $\phi' = dN/d\log M$ (e.g. Annunziatella et al., 2014; van der Burg et al., 2020), or through logarithmic mass $M' = \log(M)$ (van der Burg et al., 2018), shown in Eq. 3.2 and Eq. 3.3, respectively

$$\phi'(M)\, d\log M = \ln 10\, \phi^* \left(\frac{M}{M^*}\right)^{\alpha+1} \exp\left(-\frac{M}{M^*}\right) d\log M. \tag{3.2}$$

$$\phi'(M') = \ln 10\, \phi^* \left[10^{(M'-M'^*)(\alpha+1)}\right] \exp\left[-10^{(M'-M'^*)}\right] \tag{3.3}$$

Any of these three forms are valid for use in the likelihood function, as shown in § 3.2.1.

In our model, the parameters M^* and α, which parameterize the exponential cut-off and the low-mass slope, respectively, are extended to become functions of cluster-centric radius R and redshift z, with a general form

$$\alpha = \alpha(R, z) \tag{3.4}$$
$$M^* = M^*(R, z). \tag{3.5}$$

We propose a functional form for them as a linear combination of redshift and radius terms

$$\alpha(r', z') = \alpha_\circ + a_\alpha r' + b_\alpha z' + c_\alpha z' r' \tag{3.6}$$
$$\log M^*(r', z') = \log M^*_\circ + a_M r' + b_M z' + c_M z' r', \tag{3.7}$$

where $r' = r - 1$, $r = R/R_{200}$, and $z' = (z - z_\circ)$. This ensures the SMF parameters reduce to $M^*_\circ$ and $\alpha_\circ$ when $R = R_{200}$ and $z = z_0$. We center our sample at $z_\circ = 1.1$, around the mean of our redshift range.

3.2 Likelihood Function

We define the likelihood as $\mathcal{L} = \prod_{i=1}^{N} \mathcal{L}_i$, where $\mathcal{L}_i$ is the likelihood calculated for each galaxy and is constructed as a product of two independent terms

$$\mathcal{L}_{i,x} = \mathcal{L}_{M,i,x} \times \mathcal{L}_{R,i,x}, \tag{3.8}$$

where i is the galaxy index and the galaxy type (red or blue) is specified by $x = \{r, b\}$. We present each term separately.

3.2.1 Stellar mass dependence, $\mathcal{L}_{M,i,x}$

The first term of Eq. 3.8 considers a galaxy in a given cluster cl with a redshift z, at a fixed radius R, and determines how likely that galaxy would be drawn from a mass distribution with a given set of SMF shape parameters. Following Malumuth & Kriss (1986) and Oegerle et al. (1986) we have the form

$$\mathcal{L}_{M,i} = \frac{\phi(M_i)dM}{\int_{M_{\rm lim}}^{\infty} \phi(M)dM} = \frac{\frac{1}{M^*}\left(\frac{M}{M^*}\right)^{\alpha} \exp\left(-\frac{M}{M^*}\right) dM}{\Gamma\left(1+\alpha, M_{\rm lim}/M^*\right)}. \tag{3.9}$$

Note that the normalization parameter, ϕ^* (in Eq. 3.1), cancels out, leaving a function that depends only on the parameters M^* and α. dM is a constant that is irrelevant for maximizing the likelihood, so we drop it for simplicity.

As mentioned previously, one can equivalently define the likelihood using the logarithmic form (Eq. 3.2) and see that the original likelihood form can be recovered:

$$\mathcal{L}'_{M,i} = \frac{\phi'(M'_i)dM'}{\int_{M'_{\rm lim}}^{\infty} \phi(M')dM'} = \frac{\ln(10)\left(\frac{M}{M^*}\right)^{(1+\alpha)} \exp\left(-\frac{M}{M^*}\right) d\log(M)}{\Gamma\left(1+\alpha, M_{\rm lim}/M^*\right)} \tag{3.10}$$

$$= \frac{\frac{1}{M^*}\left(\frac{M}{M^*}\right)^{\alpha} \exp\left(-\frac{M}{M^*}\right)}{\Gamma\left(1+\alpha, M_{\rm lim}/M^*\right)} \ln(10) M d\log(M) = \mathcal{L}_{M,i} \ln(10) \frac{M d\log(M)}{dM} = \mathcal{L}_{M,i}, \tag{3.11}$$

where the last step follows from $d\log M = \frac{dM}{M \ln 10}$. To reiterate, while not explicitly shown in the equations above, the parameters α and M^* are functions of cluster-centric radius R, redshift z, and galaxy type x, as described in § 3.1.

3.2.2 Radial dependence, $\mathcal{L}_{R,i,x}$

The second term of Eq. 3.8 gives the likelihood of finding galaxy i of type x at a given radius R in cluster cl. This depends only on the radial distribution of that galaxy type, in that cluster – not the stellar mass. Like Eq. 3.9, we begin with the general form:

$$\mathcal{L}_{R,i,x} = \frac{2\pi R_i \, \varsigma(c_x, R_i) dR}{\int_0^{R_{max}} 2\pi R \, \varsigma(c_x, R) dR}. \tag{3.12}$$

We assume the radial profile as a projected NFW, with a different concentration parameter for the red and blue populations: c_r and c_b, respectively. To separate out the normalization from the radial dependence we write the projected surface density as

$$\varsigma(c_x, R_i) = \Sigma_x^* \Sigma(c_x, R_i). \tag{3.13}$$

Having a different profile for each population expands the denominator to be the sum of the integrals of these profile, with the form

$$\mathcal{L}_{R,i,x} = \frac{2\pi\Sigma_x^*\Sigma(c_x, R_i) R_i dR}{\int_0^{R_{\rm max,cl}} 2\pi\Sigma_r^*\Sigma(c_r, R) R dR + \int_0^{R_{\rm max,cl}} 2\pi\Sigma_b^*\Sigma(c_b, R) R dR}$$

$$= f_q(cl) \frac{\Sigma_x^*}{\Sigma_r^*} \frac{\Sigma(c_x, R_i) R_i dR}{\int_0^{R_{\rm max,cl}} \Sigma(c_r, R) R dR}, \tag{3.14}$$

where

$$f_q(cl) = \frac{\int_0^{R_{\rm max,cl}} 2\pi\Sigma_r^*\Sigma(c_r,R)RdR}{\int_0^{R_{\rm max,cl}} 2\pi\Sigma_r^*\Sigma(c_r,R)RdR + \int_0^{R_{\rm max,cl}} 2\pi\Sigma_b^*\Sigma(c_b,R)RdR}$$
$$= \frac{\int_0^{R_{\rm max,cl}} \Sigma(c_r,R)RdR}{\int_0^{R_{\rm max,cl}} \Sigma(c_r,R)RdR + \frac{\Sigma_b^*}{\Sigma_r^*}\int_0^{R_{\rm max,cl}} \Sigma(c_b,R)RdR}, \tag{3.15}$$

is the total red fraction for cluster cl. It should be noted that the radial variation in the quenched fraction is determined by the concentration parameters.

Writing out the likelihood function explicitly for red and blue populations gives us the forms

$$\mathcal{L}_{R,i,r} = f_q(cl)\frac{\Sigma(c_r,R_i)R_i dR}{\int_0^{R_{\rm max,cl}} \Sigma(c_r,R)RdR} \tag{3.16}$$

$$\mathcal{L}_{R,i,b} = [1-f_q(cl)]\frac{\Sigma(c_b,R_i)R_i dR}{\int_0^{R_{\rm max,cl}} \Sigma(c_b,R)RdR}. \tag{3.17}$$

It can be seen that the radial likelihood term depends only on the parameters f_q, c_r, and c_b. We further parameterize and expand the quenched fraction to be a function of redshift and cluster velocity dispersion, which we use as a proxy for dynamical mass, with the form

$$f_q = f_{q,0}(1+z')^{q_a}(1+q_b\sigma') \tag{3.18}$$

where $\sigma' = (\sigma/\sigma_\circ)^3$ and $z' = (z - z_\circ)$. Again we take both $z_\circ$ and $\sigma_\circ$ to be representative of the median of the sample at $z_\circ = 1.1$ and $\sigma_\circ = 500$km/s.

The function $\varsigma(c,R)$ and its corresponding integral have analytic expressions. We use the form from Łokas & Mamon (2001) (although similar forms can be found in Bartelmann (1996), etc.), however, we use the slightly different notation of Eq. 3.13, with a variable change of $r = R/R_{200}$, with

$$\Sigma(c,r) = \frac{1-|c^2r^2-1|^{-1/2}h(1/cr)}{(c^2r^2-1)}, \tag{3.19}$$

where $c = R_{200}/r_s$ is the concentration parameter, and

$$h(x) = \begin{cases} \cos^{-1}(x) & \text{if } r > \frac{1}{c} \\ \cosh^{-1}(x) & \text{if } r < \frac{1}{c} \end{cases}. \tag{3.20}$$

The relative normalization terms $\Sigma_x^*(c)$ are not present in Eqs. 3.16 and 3.17 as they are instead subsumed by f_q. It should be noted that the overall normalizations of the red population for each cluster could also be fit as a set of free parameters, as discussed in Appendix A. This was not done within this project, but it would allow for an alternative method of exploring the quenched fraction dependence on cluster richness.

The integral over R can be solved analytically, again using the form from Łokas & Mamon (2001):

$$\int_0^R \Sigma(R) R dR = \frac{R_{200}^2}{c^2} \left[\frac{h\left(\frac{1}{cr}\right)}{|c^2 r^2 - 1|^{1/2}} + \ln\left(\frac{cr}{2}\right) \right], \tag{3.21}$$

which, when evaluating to the limit of R_{200} simplifies to

$$\int_0^{R_{200}} \Sigma(R) R dR = \frac{R_{200}^2}{c^2} \left[\frac{h\left(\frac{1}{c}\right)}{|c^2 - 1|^{1/2}} + \ln\left(\frac{c}{2}\right) \right]. \tag{3.22}$$

3.2.3 Combined Likelihood

The final likelihood is the product of the mass and radial likelihood terms. The form for a red galaxy is stated below, given in a logged form to match the output used in the `emcee` routine:

$$\begin{aligned} \log \mathcal{L}_{i,r} = & \log \left[\frac{1}{M^*} \left(\frac{M_i}{M^*} \right)^{\alpha} \exp\left(-\frac{M_i}{M^*} \right) dM \right] + \log\left[\Sigma(c_r, R_i) R_i\right] - \log \Gamma\left(1 + \alpha, \frac{M_{\mathrm{lim(cl)}}}{M^*}\right) \\ & + \log f_q(cl) - \log \left[\int_0^{R_{\mathrm{max,cl}}} \Sigma(c_r, R) R dR \right], \end{aligned} \tag{3.23}$$

where the top line contains quantities that have to be evaluated for every galaxy (again remembering that α and M^* are evaluated for the specific R_i, z_i for each galaxy), and the bottom line contains quantities that have to be evaluated once for each cluster.

For blue galaxies, the form is slightly altered:

$$\begin{aligned} \log \mathcal{L}_{i,b} = & \log \left[\frac{1}{M^*} \left(\frac{M_i}{M^*} \right)^{\alpha} \exp\left(-\frac{M_i}{M^*} \right) dM \right] + \log\left[\Sigma(c_b, R_i) R_i\right] - \log \Gamma\left(1 + \alpha, \frac{M_{\mathrm{lim(cl)}}}{M^*}\right) \\ & + \log\left[1 - f_q(cl)\right] - \log \left[\int_0^{R_{\mathrm{max,cl}}} \Sigma(c_b, R) R dR \right]. \end{aligned} \tag{3.24}$$

This likelihood structure results in nine free parameters to be fit for each population (red and blue), in addition to the three parameters in f_q. This results in a total of 21 parameters for the whole model. The priors and posteriors for each parameter is shown in Table 4.1. The high number of parameters were not expected to all be informative for the sample size we have. As discussed in § 4.3, we explore a minimal set of these parameters and test the significance of additional parameters using the Bayesian Information Criterion (BIC).

3.2.4 Weight incorporation

In the likelihood described here, we assume the sample is complete and unbiased over the cluster areas A and for all stellar masses M. However, as discussed in § 2.3, the majority of our sample members are based on photometric redshifts, and so we formulate a weight term to rectify this.

We adopt the same approach taken in vdB20 to incorporate the weights in the likelihood, which is to apply them to the log likelihood. This gives us the form

$$\log \mathcal{L}'_i = w_i \log \mathcal{L}_i. \tag{3.25}$$

Thus the final form of the likelihood is:

$$\log \mathcal{L} = \sum_{i=1}^{N_g} w_i \left[\log \mathcal{L}_{M,i,x} + \log \mathcal{L}_{R,i,x}\right]. \tag{3.26}$$

3.3 Model Validation

We tested the validity of the model through its ability to recover the parameters of mock samples. This was done as an iterative process, with samples being drawn from distributions using an increasing amount of the parameters we were interested in recovering.

Initially, galaxy cluster-centric radial values are drawn from the probability density functions (PDFs) of projected NFW profiles with the corresponding concentration values. As the redshift of each galaxy is set to that of its parent cluster, discrete redshifts distributions were created depending on number of desired clusters and their relative normalizations, giving the mock sample galaxy redshifts. These radial and redshift values are evaluated with the mock sample parameters for the α and M^* values, to dictate the shape

of the Schechter function (see Eqs. 3.6 and 3.7). Then the mock stellar mass values are drawn the corresponding Schechter PDF for each radial and redshift combination. This gives mass, radius, and redshift values for each galaxy in the mock sample.

The entire set of 21 parameters is then fit to each sample, regardless of the size of the chosen set of mock sample parameters. This allowed us to validate that the model could recover null parameters correctly. Figure 3.1 shows the posterior distributions and parameter recovery of one of these mock samples, with the values of the initial parameter set overlaid in red. Multiple realizations of the same mock sample parameter sets were fit to confirm there was no bias within the parameter recovery.

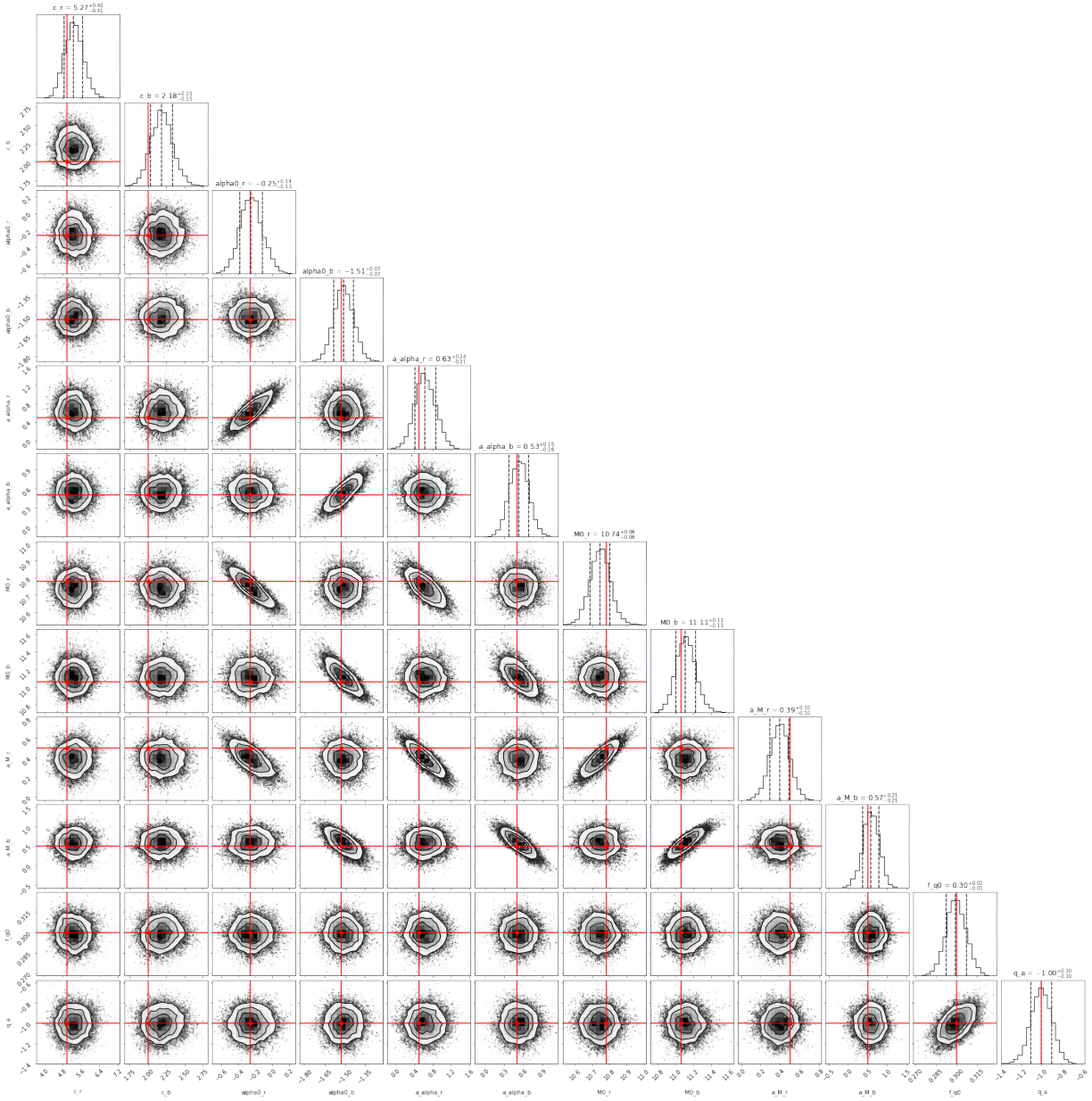


Figure 3.1: Corner plot of parameter recovery from a mock dataset. The figure validates that the parameter recovery of the model, with all the true parameter values within the 1-σ posterior range of the recovered parameter values, as indicated with the red dots at the center of each red cross. This specific fit was run on a set of 10,000 samples for 1500 iterations and 50 walkers.

Chapter 4

Results

We fit the 21 parameter model to the sample of 1606 galaxies described in § 2 using the MCMC Ensemble sampler `emcee` (Foreman-Mackey et al., 2013). The input for the model is the set of galaxy stellar masses, cluster-centric radii, and their parent cluster redshift. Other inputs include the stellar mass limit and virial radius of each cluster. The fit was completed using 50 walkers, and 3000 iterations after the burn-in period of 1000 iterations. The posterior values and their 1-σ distributions are given in Table 4.1, along with the prior ranges they were evaluated on.

The priors were set as uniform distributions with conservative ranges such that they were not dominating the parameter space the posteriors converged on, as can be seen in the complete corner plot in Figure 4.1. The ranges and initial values for the non radial and redshift dependent parameters were motivated by the fit values of the models in vdB20 and Biviano et al. (2021). In addition, the prior range for the quenched fraction normalization term ($f_{q,\circ}$) was set so the range of the overall quenched fraction function (Eq. 3.15) was always [0,1].

In this chapter we present the fits of the model and show how they describe the relationships of the galaxies in these clusters. We begin by considering and comparing some global properties of the sample that have already been determined in earlier works, including the projected radial profiles and the quenched fraction. In the next sections we consider how the shape of the SMFs of both populations vary with radial distance and redshift, in order for us to gain further insight into these trends.

4.1 Radial Profiles and Quenched Fraction

In Figure 4.2, we show the global surface density profiles of the red and blue populations constrained by their respective concentration values. Overlaid are the profiles described by the concentration values that were fit for in Biviano et al. (2021). There is good agreement between their quiescent value and ours (5.1±0.9 and 6.0±0.9, respectively), and a 2.4-σ discrepancy between their star-forming value and ours (0.7±0.4 and 2.06±0.4, respectively). However, in their work they fit concentration values for a binned split in redshift, and fit a value for their higher redshift bin that is more consistent with our value (1.5±1.0). It should be noted that their sample does not include the 3 highest redshift GOGREEN clusters that our sample does (SpARCS-0219, SpARCS-1034, and SpARCS-1033), and they use the BCG for the position of all their cluster centres, and do not include the correction we use for SpARCS-1047 and SpARCS-1051. Nevertheless, in both sets of fit values the quiescent profile has a steeper slope than the star-forming, which corresponds to a quiescent dominated core region ($f_q > 0.5$), which is shown explicitly in later figures.

Figure 4.3 shows the quenched fraction of the sample by stellar mass. The trend has a tight linear correlation that increases from 20% at the lower mass limit of the sample, to completely quenched at the highest mass bins. This trend is consistent with the form found in vdB20 and other literature (Peng et al., 2010; Muzzin et al., 2012; van der Burg et al., 2018). The values are compared to the quenched fraction values from the field SMFs from McLeod et al. (2021), evaluated at the mean redshift of our sample. The cluster quenched fraction is elevated above the field levels across the entire mass range of the sample.

Figure 4.4 shows the quenched fraction as a function of cluster-centric radius. The sample points are split into two redshift bins, along with the analytic function being evaluated for the mean redshifts for each of those bins. Overall, both forms have a strong radial correlation, with the quenched fraction increasing rapidly with proximity to the cluster core. This agrees with the idea of increased quenching due to increased local density or environmental effects, shown in previous literature (Kauffmann et al., 2004; Peng et al., 2010; Kawinwanichakij et al., 2017; Pintos-Castro et al., 2019). The figure is also overplotted with the global quenched fraction of the field (evaluated at the mean redshift of the sample), following the fit data from McLeod et al. (2021). The quenched fraction of the outer regions of the clusters is mildly enhanced compared to the field, which increases strongly with decreased radius, with the cluster cores having a highly elevated quenched fraction in comparison. The redshift split of the fit functions also gives an indication of a slight normalization increase in quenched fraction for all radii with a decrease in redshift. However, the large errors on both the fits and the confidence intervals of the binned points show this evolution is not highly significant.

The redshift evolution is explicitly shown in Figure 4.5, which shows the fit of the quenched fraction as a function of redshift (Eq. 3.15). It shows a slight increase of quenched fraction (but of low significance) with a decrease in redshift, which leads to the effect in Figure 4.4. The field quenched fraction as a function of redshift is shown as well, again taken from McLeod et al. (2021). Our model fits a quenched fraction trend that is consistently elevated from the field values at $\sim$ 3-σ levels, which is consistent with the previous literature mentions who showed that galaxy clusters exhibit increased quenching rates. Also shown is the binned quenched fraction values of the individual clusters in the sample. The dispersion they exhibit between each other is large compared to the trend with redshift, which indicates that redshift is not the main driver between their quenched fraction differences. In addition, the significant scatter does not seem to be fully captured by the uncertainty in the model.

Since the scatter between the clusters is not fully explained by their redshift differences, we also consider whether there is a dependence on their halo mass. We use the velocity dispersion values (see § 3.2.2) as a proxy for the dynamical mass of the clusters. Figures 4.6 and 4.7 show the relationship of the quenched fraction with the velocity dispersion of the cluster. Figure 4.6 directly shows the quenched fraction as a function of velocity dispersion, and like Figure 4.5, shows the relationship against the quenched fraction of the individually binned clusters. The fit exhibits no significant dependence of global quenched fraction on cluster velocity dispersion, and again the large variation on a cluster-to-cluster basis indicates velocity dispersion is not the main parameter to describe these differences. Figure 4.7 looks at the quenched fraction by cluster-centric radius again, but splits the sample in two velocity dispersion bins. It demonstrates no significant difference in the quenched fraction radial trends of clusters based on their velocity dispersion (although as shown in 4.6, the error in cluster velocity dispersion is large, which should be taken into account).

In Figures 4.3, 4.4, and 4.5, we showed the global quenched fraction of the sample as a function of stellar mass, cluster-centric radius, and redshift. As a consistency check we find that the data and fits shown in these match well with the trends found in Baxter et al. (2023) (who did similar analysis on just the GOGREEN clusters), with their work finding strong linear trends of increased quenched fraction with stellar mass and projected radial proximity to the cluster centre, and a weak trend of quenched fraction decrease with redshift.

Parameter	**Prior**	**Posterior**
$\alpha_{\circ,r}$	[-10 , 10]	$-0.64^{+0.29}_{-0.28}$
$\alpha_{\circ,b}$	[-10 , 10]	$-1.23^{+0.23}_{-0.23}$
$a_{\alpha,r}$	[-10 , 10]	$-0.32^{+0.40}_{-0.40}$
$a_{\alpha,b}$	[-10 , 10]	$-0.02^{+0.35}_{-0.38}$
$b_{\alpha,r}$	[-10 , 10]	$1.20^{+1.71}_{-1.48}$
$b_{\alpha,b}$	[-10 , 10]	$0.44^{+1.18}_{-1.18}$
$c_{\alpha,r}$	[-10 , 10]	$0.78^{+2.33}_{-2.27}$
$c_{\alpha,b}$	[-10 , 10]	$0.30^{+1.97}_{-1.98}$
$M^*_{\circ,r}$	[5 , 30]	$10.65^{+0.13}_{-0.12}$
$M^*_{\circ,b}$	[5 , 30]	$10.78^{+0.21}_{-0.17}$
$a_{M^*,r}$	[-10 , 10]	$-0.27^{+0.18}_{-0.18}$
$a_{M^*,b}$	[-10 , 10]	$-0.26^{+0.33}_{-0.31}$
$b_{M^*,r}$	[-10 , 10]	$-0.44^{+0.56}_{-0.56}$
$b_{M^*,b}$	[-10 , 10]	$-0.25^{+0.87}_{-0.93}$
$c_{M^*,r}$	[-10 , 10]	$0.00^{+0.86}_{-0.81}$
$c_{M^*,b}$	[-10 , 10]	$0.37^{+1.67}_{-1.72}$
c_r	[0 , 20]	$6.00^{+0.95}_{-0.87}$
c_b	[0 , 20]	$2.06^{+0.44}_{-0.38}$
$f_{q,\circ}$	[0 , $1^{(a)}$]	$0.49^{+0.03}_{-0.03}$
q_a	[-5 , 5]	$-0.41^{+0.23}_{-0.23}$
q_b	[-5 , 5]	$0.00^{+0.01}_{-0.01}$

Table 4.1: An overview of the 21 parameters, the prior ranges they were evaluated on, and their best-fit posterior values with their 1-σ/68% confidence limits. The prior ranges all correspond to flat priors. $^{(a)}$The upper range of the prior for $f_{q,\circ}$ is set so the overall f_q term is less than 1.

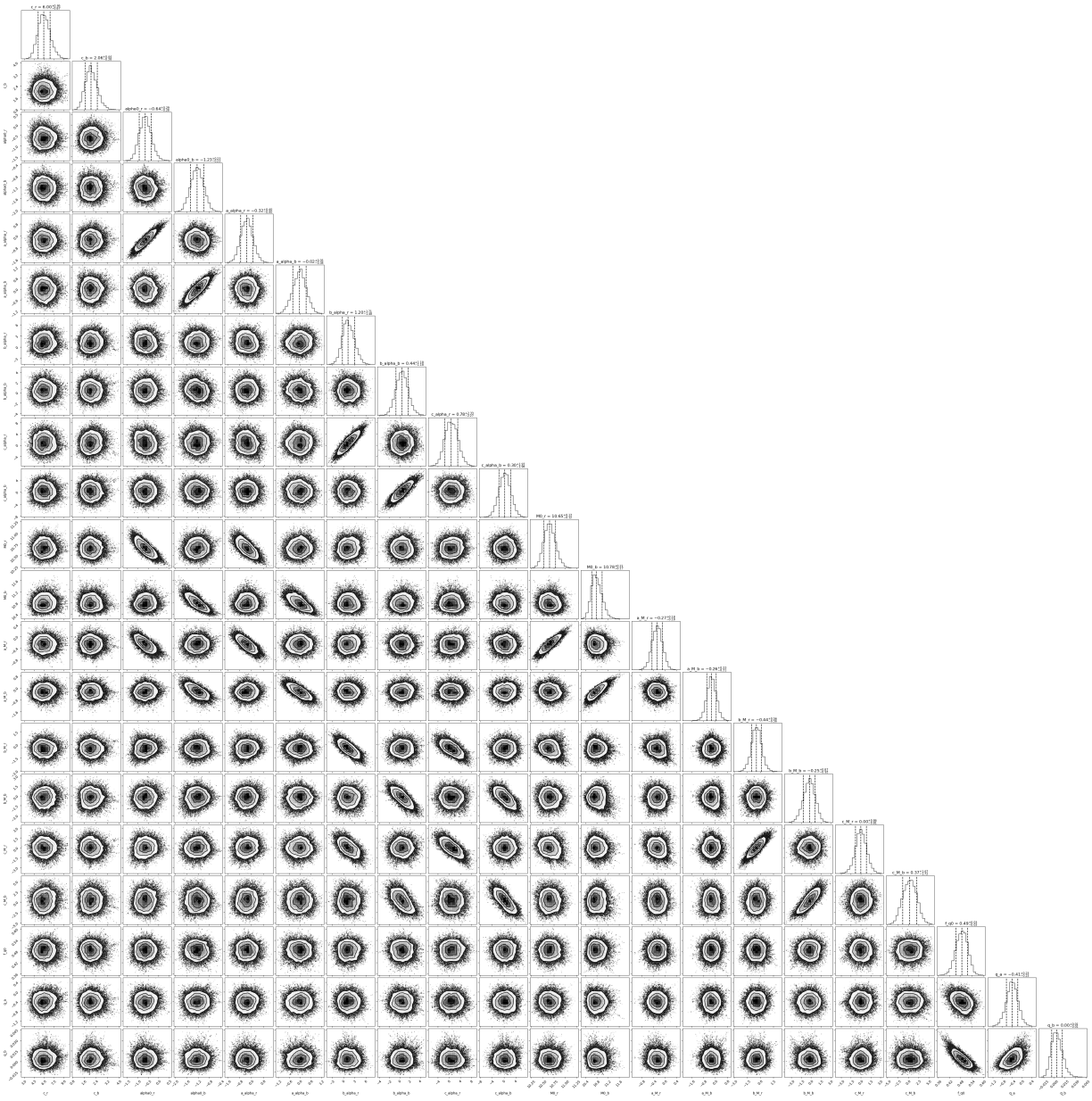


Figure 4.1: Complete corner plot of all parameters fit with the sample, corresponding to the values in Table 4.1. The 16, 50, and 84 percentiles (the 1-σ constraints) are shown with the vertical dashed lines in the 1-D histograms. The plot was constructed using the `corner` software (Foreman-Mackey, 2016).

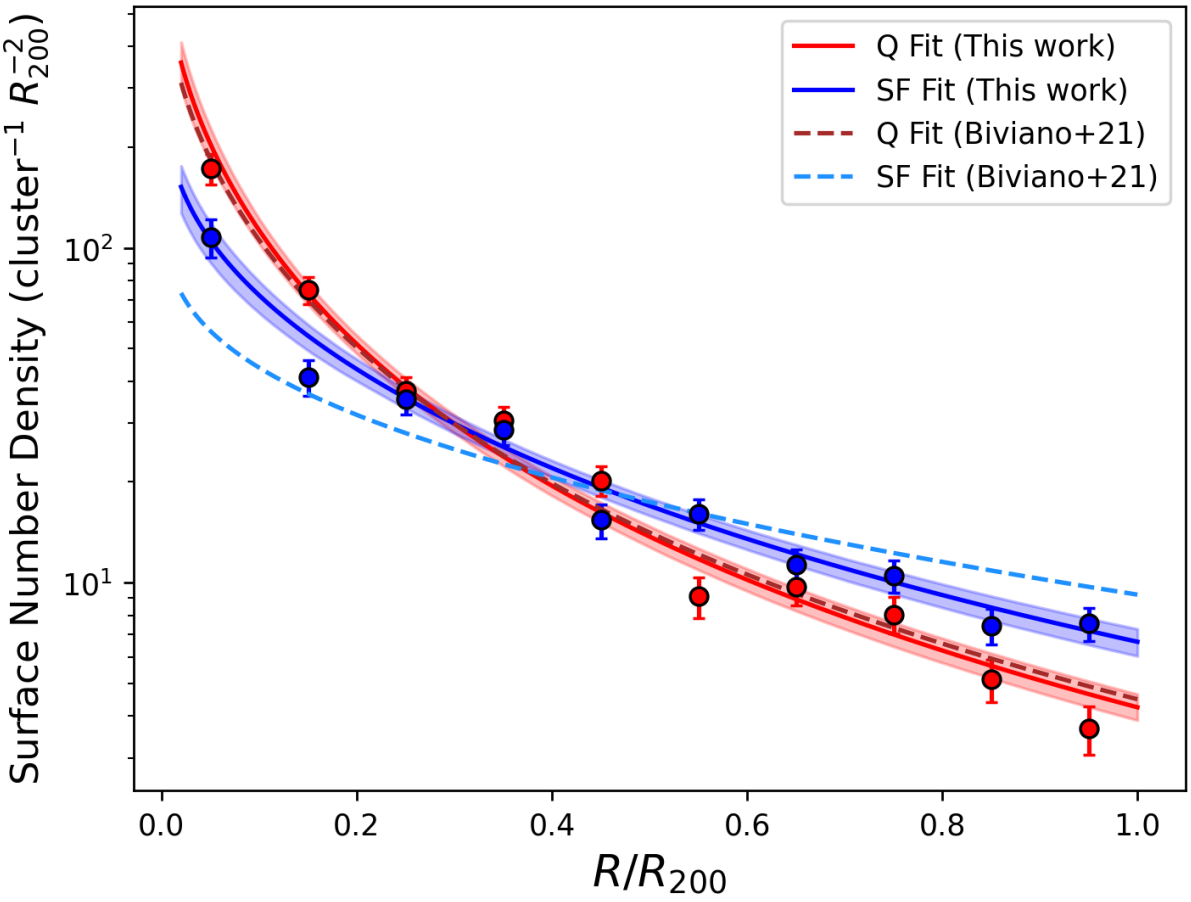


Figure 4.2: Surface number density of cluster galaxies as a function of cluster-centric radius for the quiescent and star-forming populations, with comparison to fits with the concentration values found in Biviano et al. (2021).

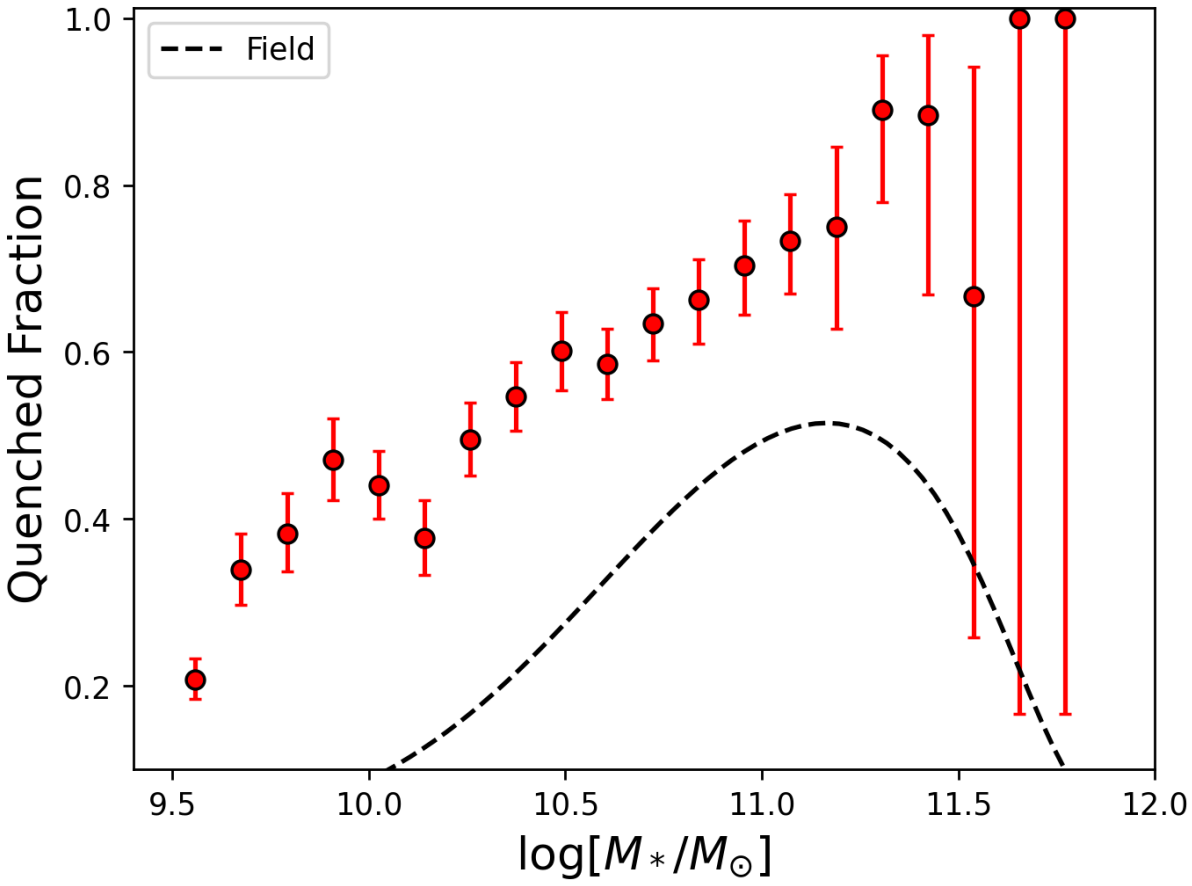


Figure 4.3: Global quenched fraction dependence on stellar mass, for all radial and redshift values. The errors correspond to the binomial confidence intervals of each binned point. The field value corresponds to the quenched fraction values of field galaxies in the redshift range of the sample, following the fits from McLeod et al. (2021).

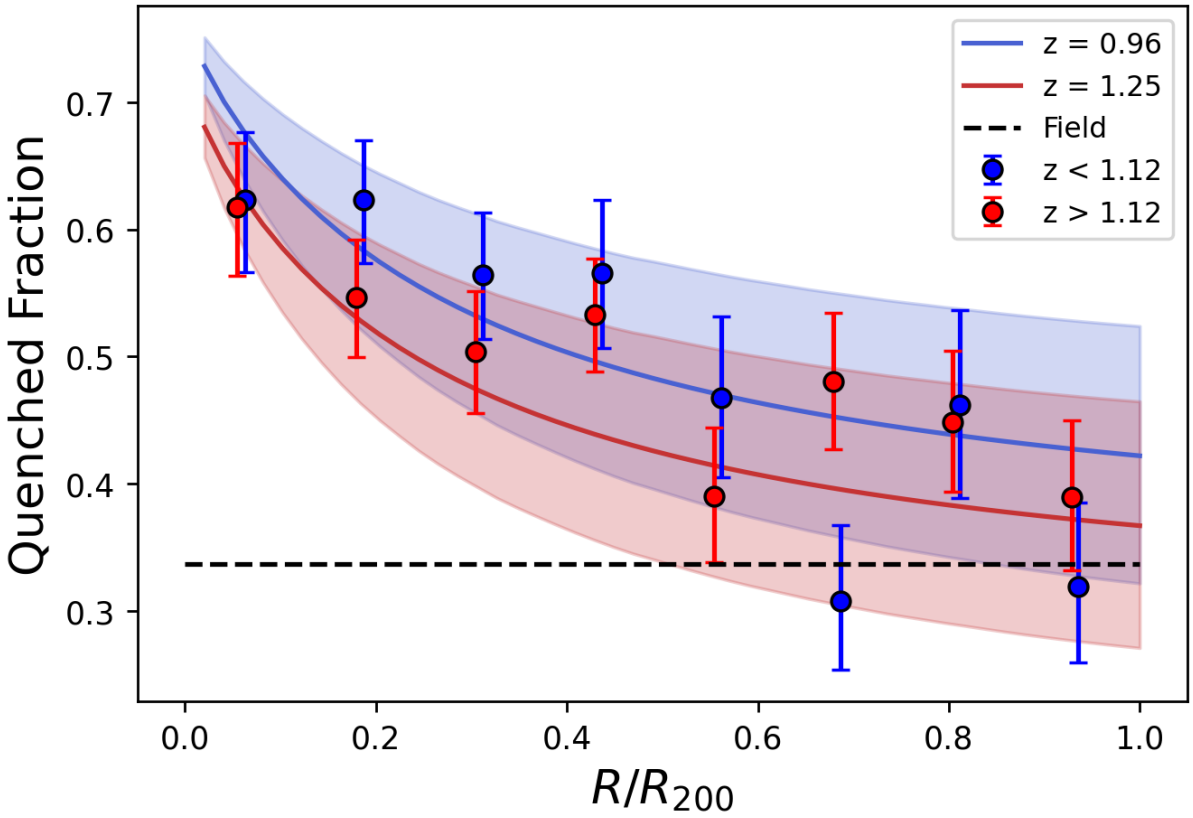


Figure 4.4: Binned points of the sample and the fit form of the quenched fraction as a function of cluster-centric radius. The sample is split into two bins based on the mean redshift of the sample ($z \simeq 1.12$). The high redshift binned points are slightly offset from their original position matching that of the low redshift binned points, for a simplified visual effect. The quenched fraction function (Eq. 3.15) is evaluated at the mean redshift values of each of the bins. The errors on the binned points are their corresponding binomial confidence intervals, and the errors on the fits are the 1-σ parameter errors. The field value is set to the global field quenched fraction value at the mean redshift of the sample following the fit functional form from McLeod et al. (2021).

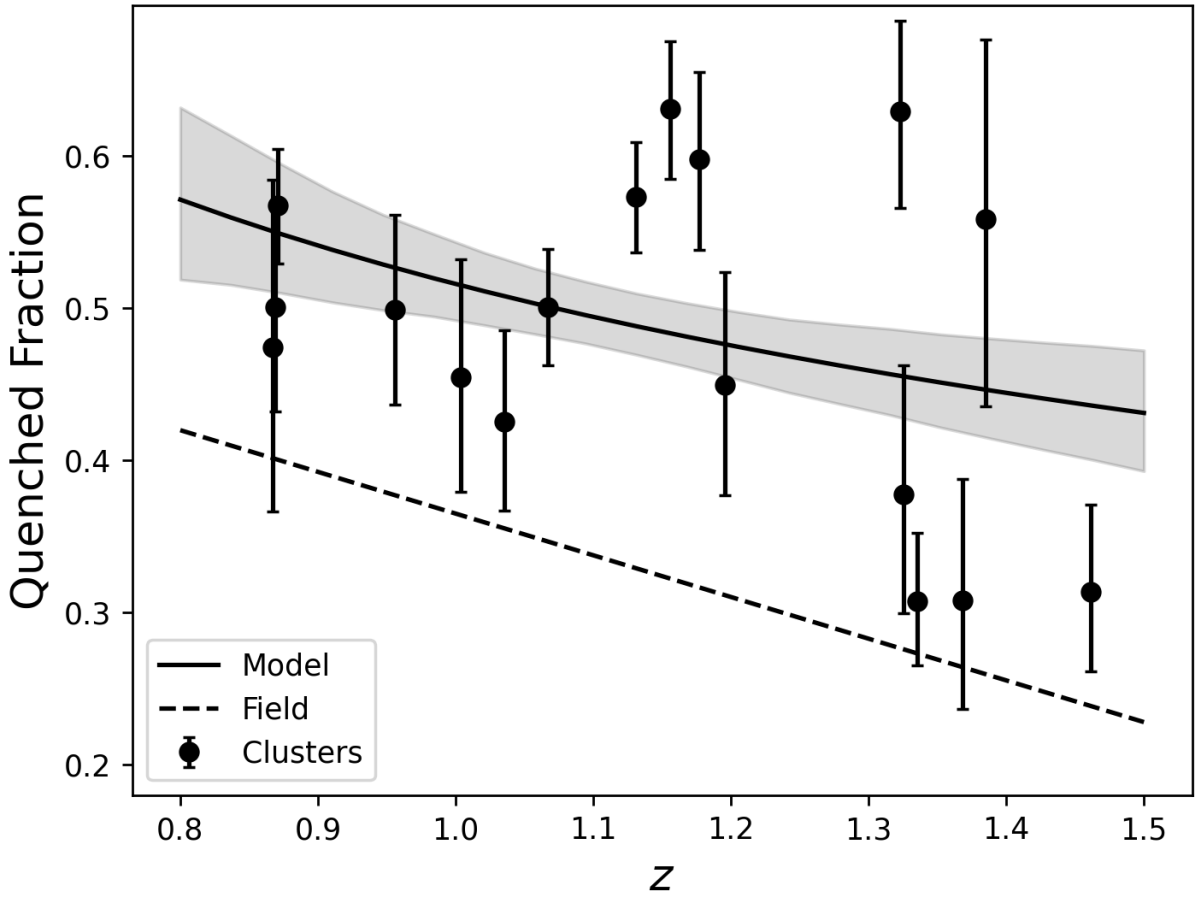


Figure 4.5: The fit quenched fraction as a function of redshift, evaluated on the mean cluster velocity dispersion of the sample ($\sigma = 891$ km/s). The errors are the 1-σ parameter errors. The binned points show the quenched fraction of the individual 17 clusters in the sample and their corresponding binomial confidence intervals. The field reference corresponds to the fit quenched fraction function from McLeod et al. (2021).

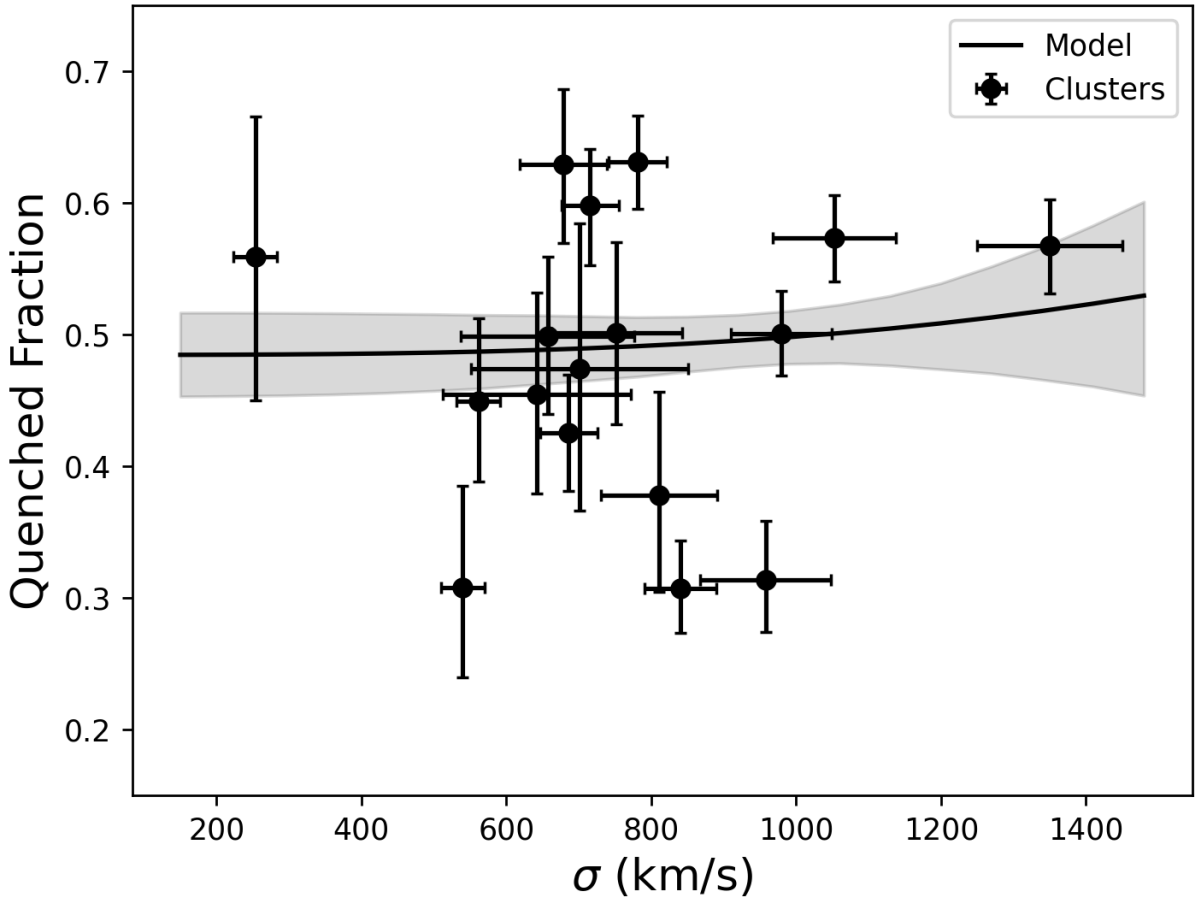


Figure 4.6: The modelled quenched fraction as a function of velocity dispersion of the clusters, including the ± 1-σ parameter uncertainties. Also shown in the binned quenched fraction of the individual clusters, with their confidence intervals as the vertical errors and their errors in velocity dispersion as their horizontal errors, with the values matching those in Balogh et al. (2021).

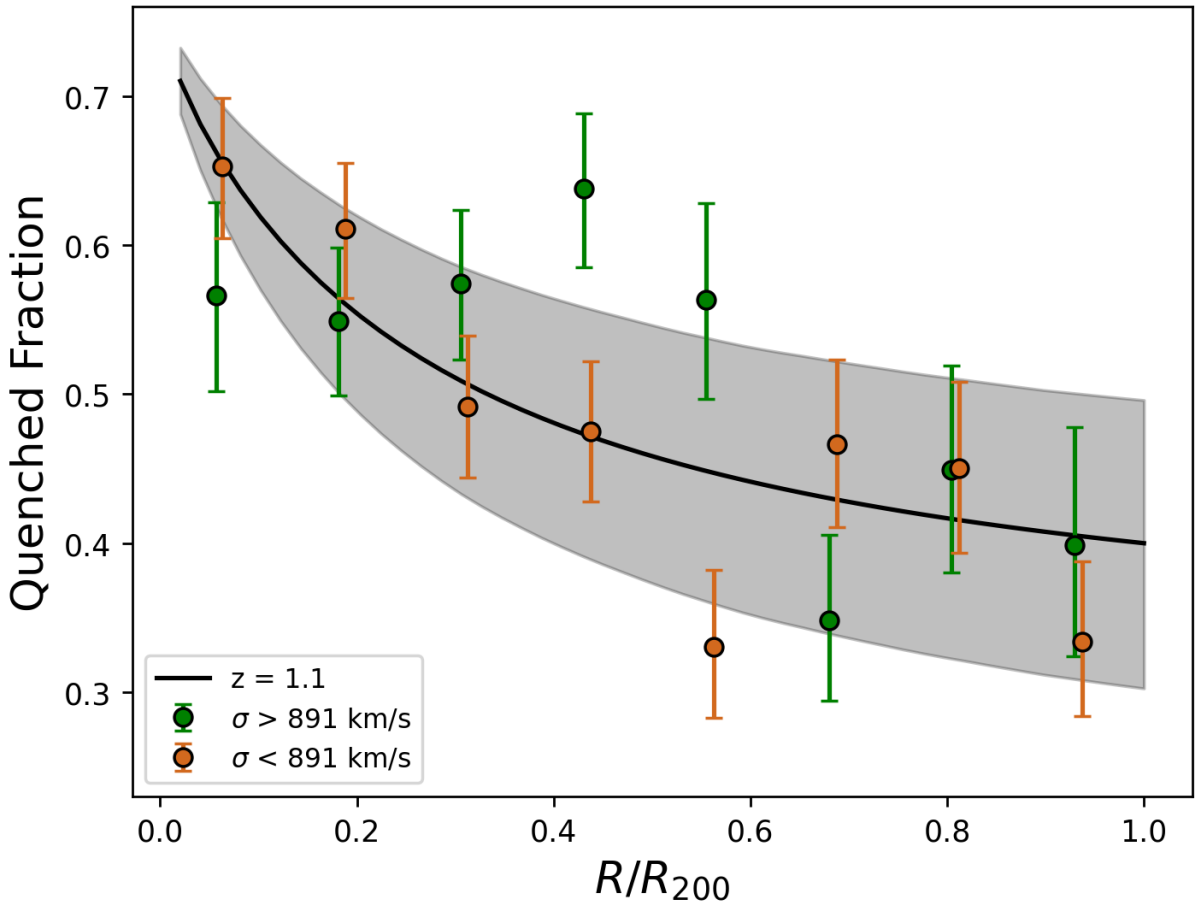


Figure 4.7: Binned points of the sample and the fit form of the quenched fraction as a function of cluster-centric radius. The sample is split into two velocity dispersion bins based on the mean velocity dispersion of the sample ($\sigma \simeq 891$ km/s). The function is evaluated at the mean redshift of the cluster ($z \simeq 1.1$), with its errors being the 1-σ parameter uncertainties. The errors on the binned points are their binomial confidence intervals.

4.2 Stellar Mass Function Fits

With the aim of the project being to model how the stellar mass functions of cluster populations are changing with radius and redshift, we divided each population (quiescent and star-forming) into subsets, in order to see how well the overall model is able to fit each of them. We broke the sample into six sub-populations: two radial regimes ($0 < R/R_{200} \leq 0.45$ and $0.45 < R/R_{200} \leq 1.0$), and three redshift regimes ($z \leq 1.05$, $1.05 < z \leq 1.25$, and $1.25 < z$), all of which had roughly equal population sizes between them. We plot the binned number density through mass for each subset, and overlay the mass function from the full model but with the global α and M^* parameters evaluated for the mean radius and redshift of each sub-sample. Additionally, we also fit a Schechter function with no radial or redshift dependency (see Eq. 3.1) to each subset, which we call the 'simple model', giving a comparison fit.

Throughout this work, the errors on the SMF binned points are Poisson errors with the relative magnitude of their weights taken into account.

4.2.1 Star-Forming Population

Figure 4.8 shows the six sub-populations of the star-forming galaxies, with the binned number density points by their stellar mass. Overlaid is both the full model and simple model fits to each sub-sample. Both fits are in good agreement with each sample, and additionally, both fits are in very good agreement with each other. One key difference between them is that the size of the parameter uncertainties on the full model is more constrained than the individual simple model fits, especially at the low and high mass ends. This is a reflection of the additional information the complete model had from its access to the entire sample.

Figure 4.9 shows the star-forming α parameter as a function of cluster-centric radius and redshift, in their respective panels. In the top panel, the fits show no radial dependence, regardless of the mean redshifts they are evaluated for. The redshift evolution is shown in the bottom panel, with the α parameter indicating a non-significant increase with redshift. Compared to the field, the fits and binned points are consistently elevated from the field α values, yet are consistent at the 1-σ level. Figure 4.10 shows the star-forming M^* parameter as a function of cluster-centric radius and redshift, in their respective panels. Both panels show a non-significant decrease of the characteristic mass with radius and redshift, with the binned points and the fits being consistent with the field values. These figures indicate

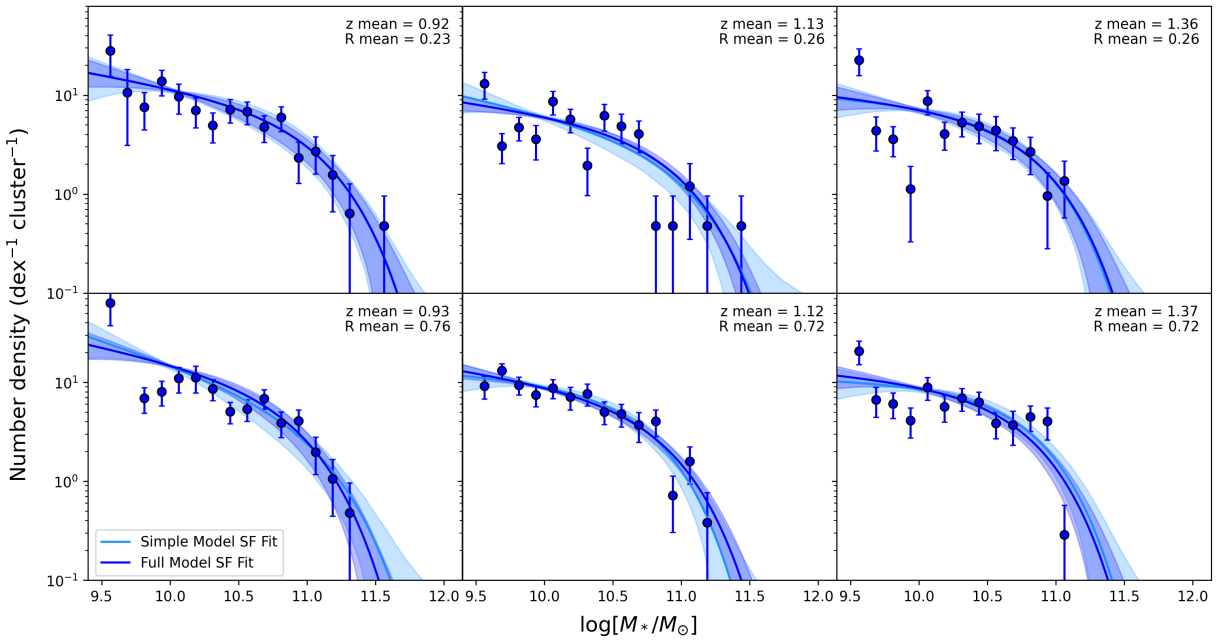


Figure 4.8: Binned number density against stellar mass points for the star-forming galaxy population through two radial bins and three redshift bins. Overlaid is the comparison of the complete model (the blue 'Full Model' fit) evaluated at the mean z and R/R_{200} values of each group (which are stated in each sub-figure), against a non radial or redshift dependent Schechter function fit for just the population in each subgroup (the light blue 'Simple Model' fit).

that the star-forming populations in the clusters do not significantly evolve or alter with environment, and are consistent with their field counterparts.

4.2.2 Quiescent Population

Figure 4.11 shows the six sub-populations of the star-forming galaxies, with the binned number density points by their stellar mass. Overlaid is both the full model and simple model fits to each sub-sample. Both fits are in good agreement with each sample, and additionally, both fits are in very good agreement with each other. Again, the major difference between them is that the size of the parameter uncertainties on the full model is more constrained than the individual simple model fits, in particular at the low mass end. This is due to the additional information that the model gained from its access to

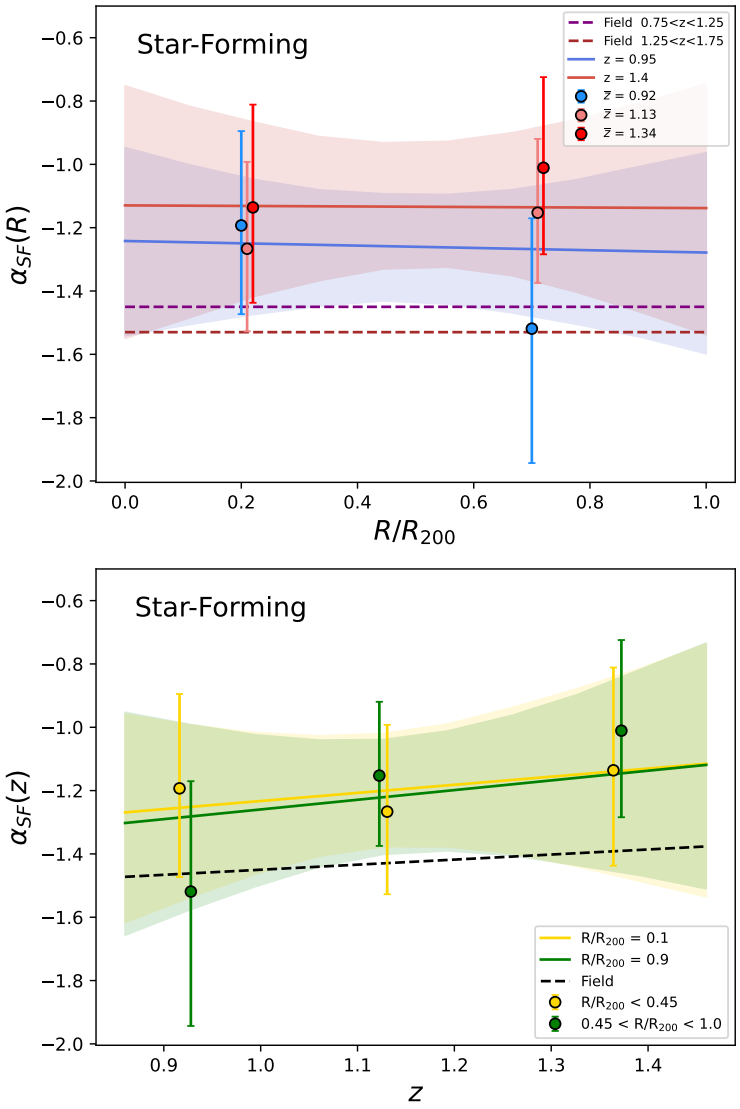


Figure 4.9: *Top*: The fit star-forming α parameters as a function of R/R_{200}, with their 1-σ parameter errors. The functions are evaluated for two constant redshifts: $z = 0.95$ (blue) and $z = 1.4$ (red), which are the edges of the range of the entire sample. *Bottom*: The fit star-forming α parameters as a function of z, with their 1-σ parameter errors. The functions are evaluated for two constant radial positions: $R/R_{200} = 0.1$ (yellow) and $R/R_{200} = 0.9$ (green). In both figures, the binned points correspond to the simple model α values and their parameter errors from the six sub-populations in Figure 4.8. In both figures, the values are compared to the star-forming field α values from McLeod et al. (2021).

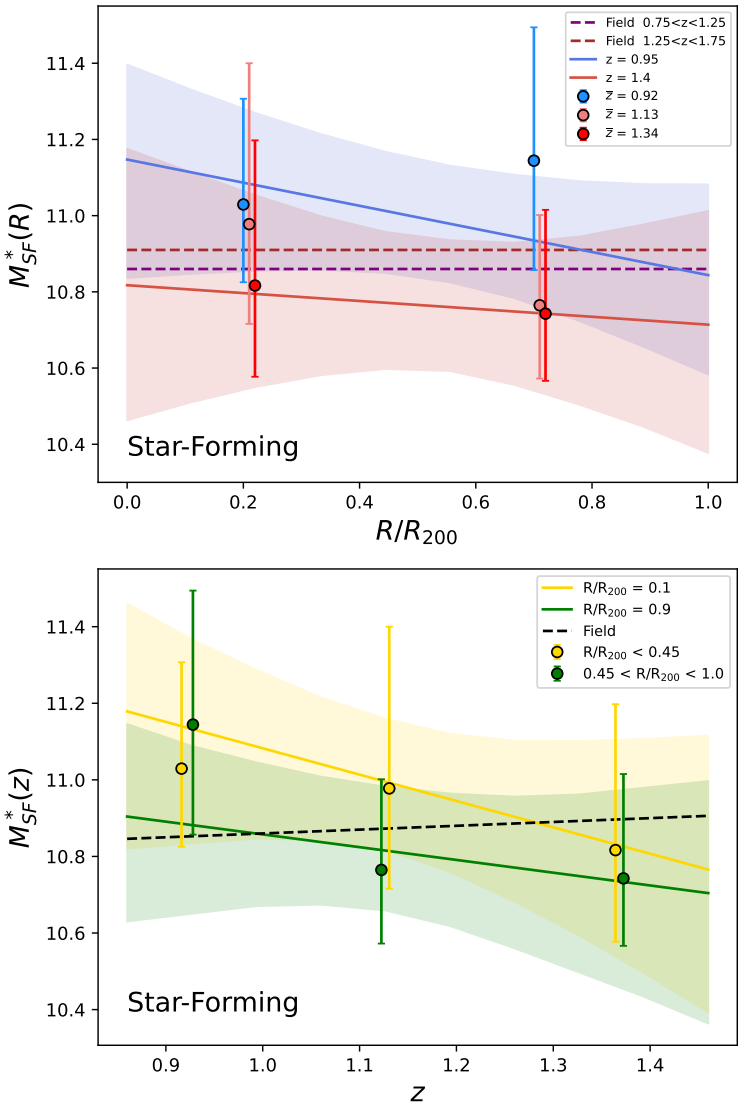


Figure 4.10: *Top*: The fit star-forming M^* parameters as a function of R/R_{200}, with their 1-σ parameter errors. The functions are evaluated for two constant redshifts: $z = 0.95$ (blue) and $z = 1.4$ (red), which are the edges of the range of the entire sample. *Bottom*: The fit star-forming M^* parameters as a function of z, with their 1-σ parameter errors. The functions are evaluated for two constant radial positions: $R/R_{200} = 0.1$ (yellow) and $R/R_{200} = 0.9$ (green). In both figures, the binned points correspond to the simple model M^* values and their parameter errors from the six sub-populations in Figure 4.8. In both figures, the values are compared to the star-forming field M^* values from McLeod et al. (2021).

the entire sample.

Figure 4.12 shows the quiescent α parameter as a function of cluster-centric radius and redshift, in their respective panels. In the top panel the fits show a significant radial dependence for the low redshift bin, with α decreasing with radius, and no radial dependence or field deviation for the high redshift bin. The bottom panel shows the redshift evolution of α, where both radial bins show increasing α values that approach the field values with an increase in redshift. Figure 4.13 shows the quiescent M^* parameter as a function of cluster-centric radius and redshift, in their respective panels. The top panel shows a moderately significant increase in M^* and deviation from field values with proximity to the cluster core. Likewise the bottom panel also shows a moderately significant increase in M^* and deviation from field values with a decrease in redshift. These figures indicate evidence that the quiescent population is not consistent with the field, and shows some moderate evolution and change with environment.

4.3 Constraining Parameters and ΔBIC

As mentioned in § 3.2.3 and evident through the fit values in Table 4.1, not all of the parameters we fit for were informative, and many of the parameters that describe the radial and redshift dependence of α and M^* are fully consistent with zero. In order to constrain the parameter set to the most significant parameters of the model, we first limit the model to a simplified base set of parameters: $\left[c_r, c_b, \alpha_{\circ,r}, \alpha_{\circ,b}, M^*_{\circ,r}, M^*_{\circ,b}, f_{q,\circ}\right]$. This base model assumes a global α and M^* value that is independent of radius and redshift in both the star-forming and quiescent populations, as well as assuming concentration values to describe the radial profiles of each population, and a single quenched fraction term that is independent of redshift or velocity dispersion. With this base model, we are able to add in additional parameters and validate their significance through the difference in the BIC measurements of each model (ΔBIC). The BIC quantifies significant improvement of the model through the addition of parameters by penalizing models by the size of their parameter space, with a form of $k * \ln(N) - 2\ln(\mathcal{L})$, where N is the sample size, k is the number of parameters, and $\mathcal{L}$ is the likelihood of that specific model (Schwarz, 1978).

A variety of parameter combinations were explored, with their BIC and ΔBIC values given in Table 4.2. Interpretation of ΔBIC values is that negative values indicate no evidence for significant improvement of the model with additional parameters, $0<\Delta\text{BIC}<2$ indicates weak evidence of significant improvement, $2<\Delta\text{BIC}<6$ indicates moderate evidence of significant improvement, $6<\Delta\text{BIC}<10$ indicates strong evidence of significant

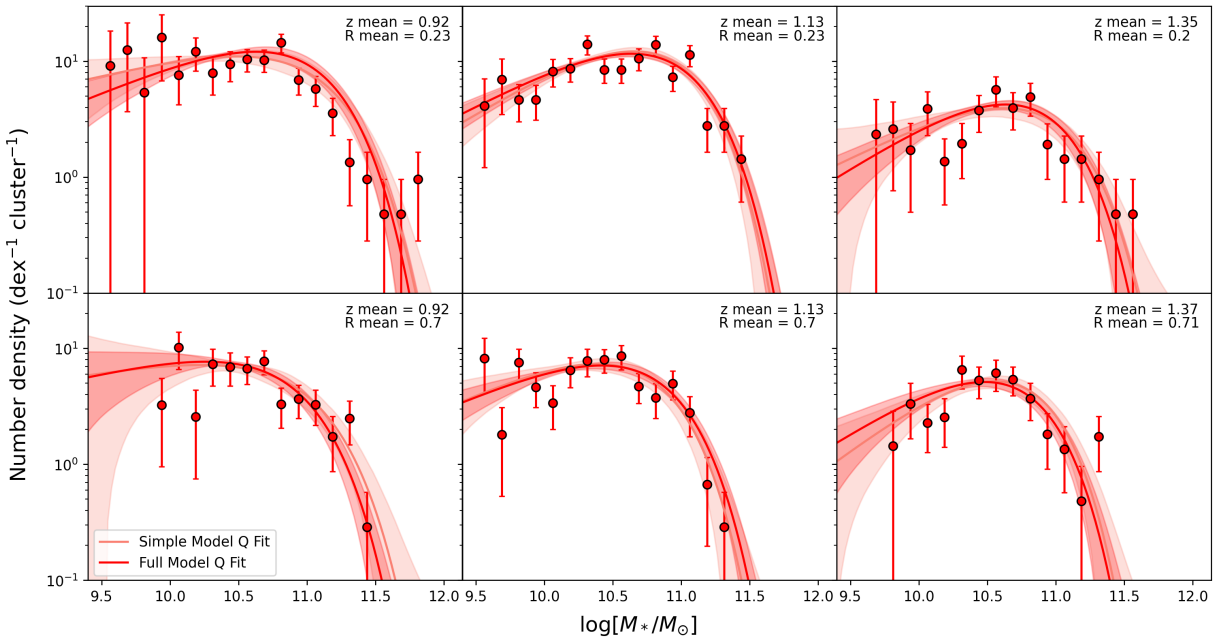


Figure 4.11: Binned number density against stellar mass points for the quiescent galaxy population through two radial bins and three redshift bins. Overlaid is the comparison of the complete model (the red 'Full Model' fit) evaluated at the mean z and R/R_{200} values of each group (which are stated in each sub-figure), against a non radial or redshift dependent Schechter function fit for just the population in each subgroup (the pink 'Simple Model' fit).

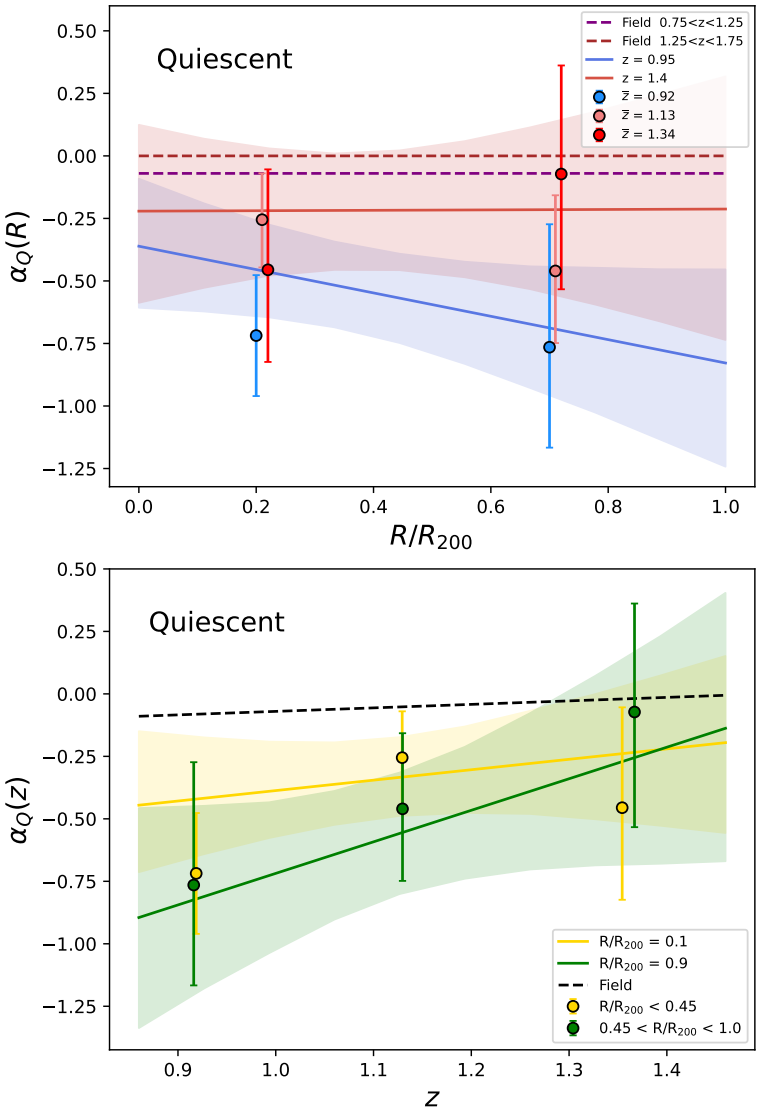


Figure 4.12: *Top*: The fit quiescent α parameters as a function of R/R_{200}, with their 1-σ parameter errors. The functions are evaluated for two constant redshifts: $z = 0.95$ (blue) and $z = 1.4$ (red), which are the edges of the range of the entire sample. *Bottom*: The fit quiescent α parameters as a function of z, with their 1-σ parameter errors. The functions are evaluated for two constant radial positions: $R/R_{200} = 0.1$ (yellow) and $R/R_{200} = 0.9$ (green). In both figures, the binned points correspond to the simple model α values and their parameter errors from the six sub-populations in Figure 4.11. In both figures, the values are compared to the quiescent field α values from McLeod et al. (2021).

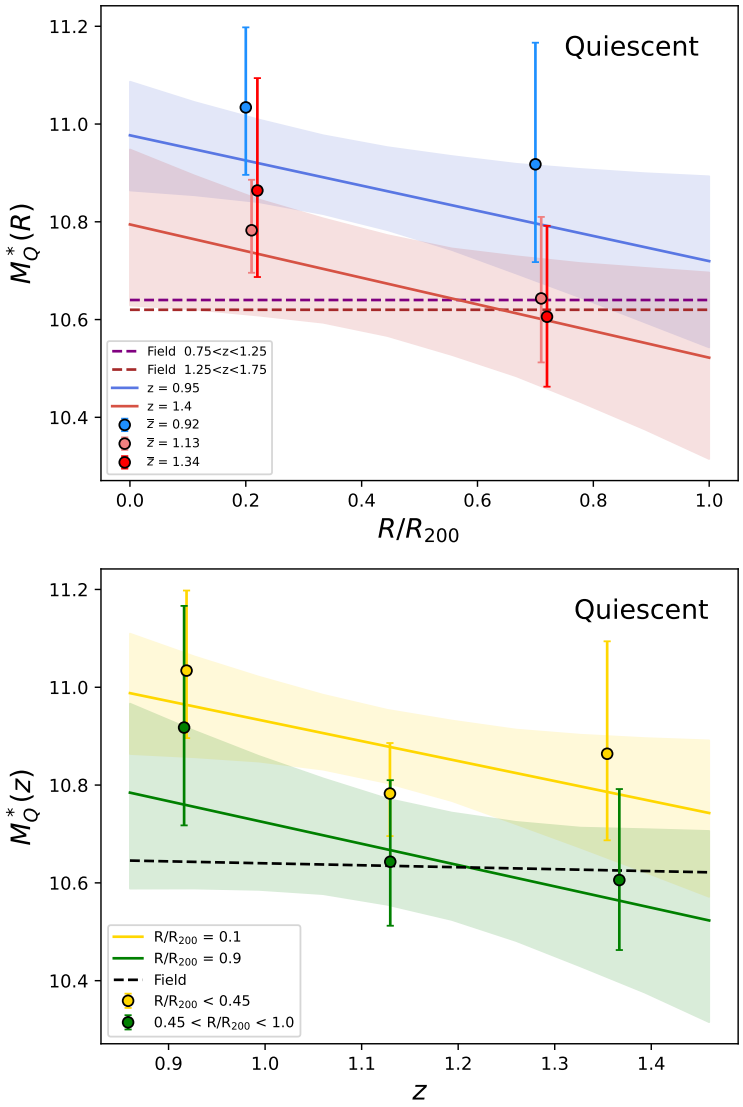


Figure 4.13: *Top*: The fit quiescent M^* parameters as a function of R/R_{200}, with their 1-σ parameter errors. The functions are evaluated for two constant redshifts: $z = 0.95$ (blue) and $z = 1.4$ (red), which are the edges of the range of the entire sample. *Bottom*: The fit quiescent M^* parameters as a function of z, with their 1-σ parameter errors. The functions are evaluated for two constant radial positions: $R/R_{200} = 0.1$ (yellow) and $R/R_{200} = 0.9$ (green). In both figures, the binned points correspond to the simple model M^* values and their parameter errors from the six sub-populations in Figure 4.11. In both figures, the values are compared to the quiescent field M^* values from McLeod et al. (2021).

improvement, and ΔBIC>10 indicates very strong evidence of significant improvement with additional parameters.

We find only two cases which have positive ΔBIC values: the addition of the radial component in the quiescent α expansion, and the addition of the radial component in the quiescent M^* expansion, which both individually present moderate evidence for a significant improvement with their addition.

Figure 4.14 shows the fit of the quiescent α as a function of radius (corresponding to the parameter subset 'Base + $a_{\alpha,r}$'). Since there is no redshift dependence within the model, there is only a single fit (unlike in Figure 4.12). With the decreased parameter space, the 1-σ parameter errors are smaller. The fit shows a strong radial dependence, with the α value increasing significantly from the cluster outskirts to the cluster core, which corresponds to a decreasing amount of quenched low mass galaxies with proximity to the core. The core α value is also the region which approaches the fit quiescent field values from McLeod et al. (2021).

Figure 4.15 shows the fit of the quiescent M^* as a function of radius (corresponding to the parameter subset 'Base + $a_{M^*,r}$'). Again there is no redshift dependence within the model, and so there is only a single fit. The 1-σ parameter errors are also much more constrained than the fit model in Figure 4.13. The fit shows a strong radial dependence, with the M^* value increasing significantly from the cluster outskirts to the cluster core, which corresponds to a increasing exponential drop-off at the high-mass end of the stellar mass functions, with proximity to the core. The cluster outskirts M^* value is also the value in the most agreement with the fit quiescent field values (again from McLeod et al. (2021)).

In summary, we find significant evidence that the SMFs of quiescent galaxies differ from the field population depending if there are in the cluster core ($R < 0.5R_{200}$) or the cluster outskirts ($R > 0.5R_{200}$). In the core the population shows an elevated characteristic mass, and in the outskirts the population shows a increased low-mass slope (dimished α). We find no significant evolution of these parameters within the redshift range of our sample. The consequences and interpretation of these results will be discussed in the next chapter.

Parameter Combination	**BIC Value**	**ΔBIC**
Base	5096.20	N/A
Base + $a_{\alpha,r}$	5092.93	**3.27**
Base + $a_{M^*,r}$	5090.23	**5.97**
Base + $b_{\alpha,r}$	5103.52	-7.32
Base + $b_{M^*,r}$	5101.86	-5.66
Base + $c_{\alpha,r}$	5103.48	-7.28
Base + $c_{M^*,r}$	5102.51	-6.31
Base + $a_{\alpha,b}$	5102.52	-6.32
Base + $a_{M^*,b}$	5101.67	-5.47
Base + $b_{\alpha,b}$	5103.40	-7.20
Base + $b_{M^*,b}$	5102.40	-6.20
Base + $c_{\alpha,b}$	5103.25	-7.05
Base + $c_{M^*,b}$	5102.39	-6.19
Base + q_a	5098.34	-2.14
Base + q_b	5101.56	-5.36
Base + $a_{\alpha,r}$ + $a_{M^*,r}$	5097.12	-0.92
All parameters	5178.85	-82.65

Table 4.2: Select combinations of model parameter subsets, along with their BIC value and their ΔBIC value relative to the 'Base' combination (given in § 4.3).

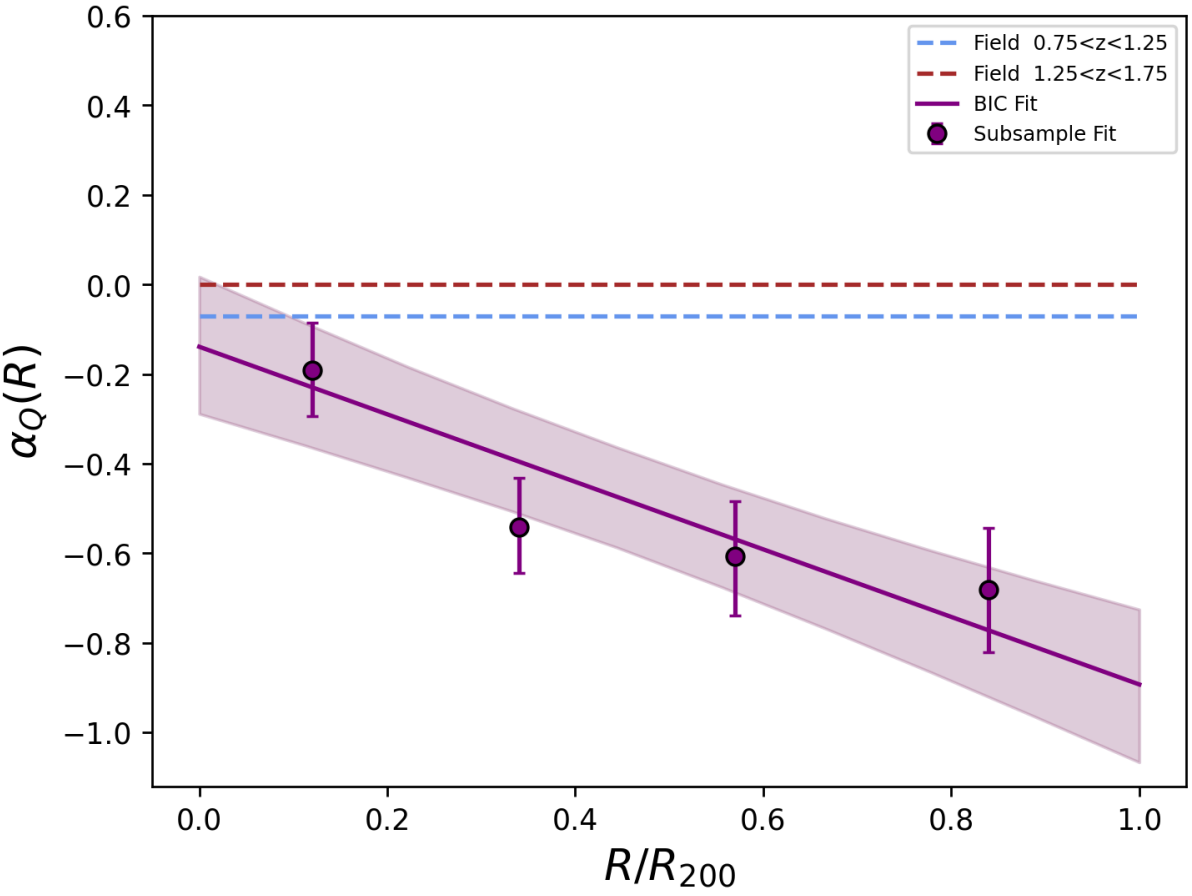


Figure 4.14: The fit quiescent α parameter as a function of R/R_{200} on the model parameter subset where the quiescent α is only allowed to vary with radius. This model configuration corresponds to 'Base + $a_{\alpha,r}$' within Table 4.2. The binned points correspond to individual fit values of four radial sub-populations (with no redshift binning). The field values from McLeod et al. (2021) are also overlaid.

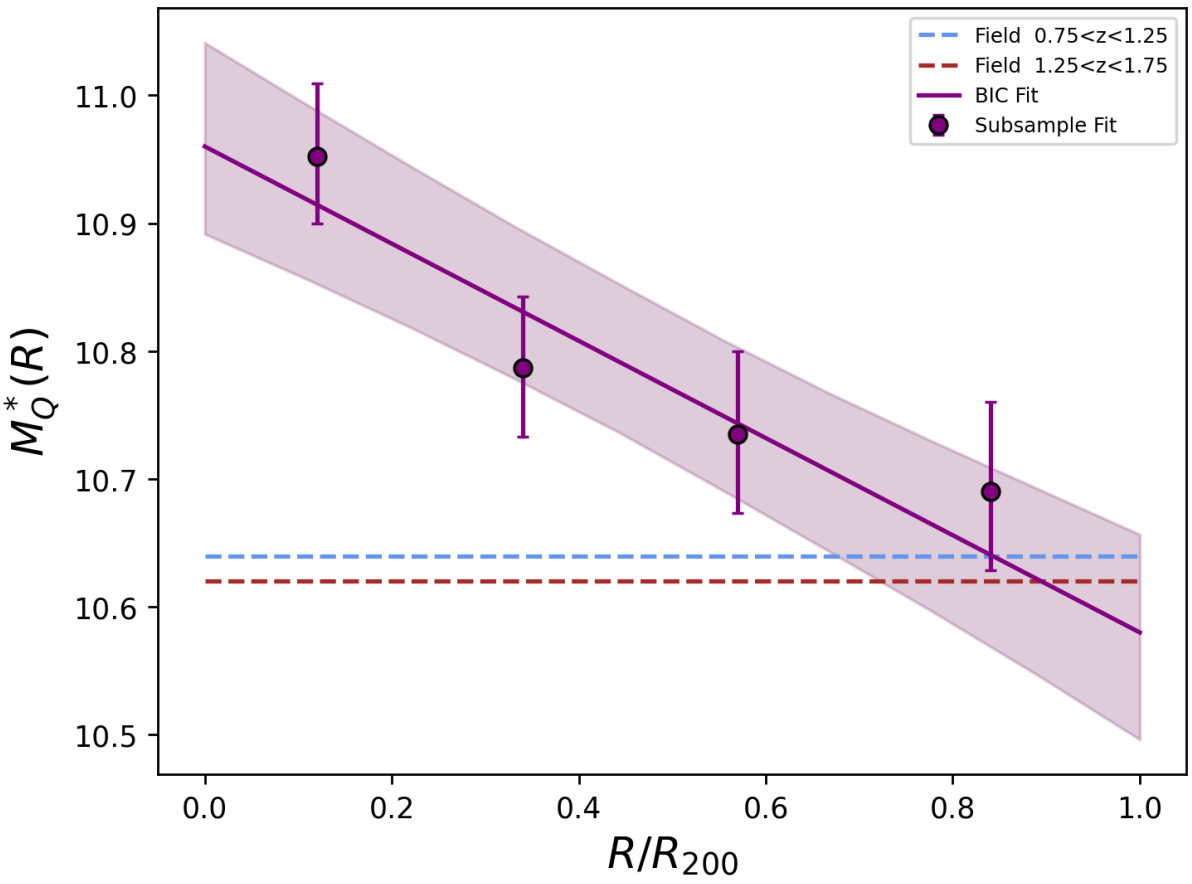


Figure 4.15: The fit quiescent M^* parameter as a function of R/R_{200} on the model parameter subset where the quiescent M^* is only allowed to vary with radius. This model configuration corresponds to 'Base + $a_{M^*,r}$' within Table 4.2. The binned points correspond to individual fit values of four radial sub-populations (with no redshift binning). The field values from McLeod et al. (2021) are also overlaid.

Chapter 5

Discussion

5.1 Literature Comparison

It is expected based on previous literature for the quenched fraction to depend on stellar mass, cluster-centric radius, and redshift (Dressler, 1980; Peng et al., 2010; Muzzin et al., 2012, 2013; Tomczak et al., 2014, 2017; Jian et al., 2017; Guglielmo et al., 2019; Pintos-Castro et al., 2019; Roberts et al., 2019; Stott, 2022; Baxter et al., 2023). Using a simple model where mass-quenching and environmental-quenching are separable (e.g. Peng et al., 2010; Muzzin et al., 2012), it is assumed the excess of quenched galaxies in clusters is built up through a mass independent conversion of the star-forming population. If this model holds true, it is necessary that the quiescent SMFs of cluster galaxies should be different from the field mass functions. Observations of low redshift clusters find a SMF difference, and this separable model is able to reproduce the observations in the local universe (Peng et al., 2010).

Observations of higher redshift clusters present a different result. The results from vdB20 show that both the quiescent and star-forming cluster SMFs at redshifts $1.0 < z < 1.4$ have no measurable difference from the shapes of their respective field populations. The conclusion they drew was that there must be some shared mechanism in both environments that results in an outcome of mass-quenching that we observe, but just at an enhanced rate in clusters (to achieve the elevated quenched fraction in these clusters). They explore possibilities including an 'early mass quenching' model with earlier formation times of the cluster member progenitors.

In Figures 4.9 and 4.10 we show that the SMF fits for the star-forming α and M^* parameters were invariant as a function of radius and redshift, as well as consistent with the

related field values. As mentioned previously, this trend is consistent through all suggested models, and has been seen in previous work through various redshift and environmental conditions (Ilbert et al., 2013; Vulcani et al., 2013; Annunziatella et al., 2014; Bundy et al., 2017; Papovich et al., 2018; Kawinwanichakij et al., 2020).

In Figures 4.14 and 4.15, we show moderately significant evidence for a dependence of α and M^* on cluster-centric radius for the quiescent population. In the cluster core, the quiescent population has an α value consistent with the field and a significantly elevated M^*, while in the cluster non-core the trend is reversed, with the quiescent population having an M^* value consistent with the field and a significantly diminished α value. In Figure 5.1 we adapt and add our results to one of the figures from Papovich et al. (2018), where they show their fits of Schechter parameters for low and high density regimes of quiescent galaxies through a redshift range of $0 < z < 2$. They use survey data from ZFOURGE (Straatman et al., 2016) and NBMS (Whitaker et al., 2011), which both cover random fields over a combined area of $\sim$1800 arcmin^2. Since their data covers field galaxies and not the rich structures that our sample does, their highest density quartile is more akin to our lowest density regime (the cluster non-core). The cores of our massive clusters represent a density regime that exceeds the environments probed in those fields, and so we denote the core parameter values differently.

The Papovich et al. (2018) data presents a strong trend in α with redshift for their most overdense environments, transitioning from a steep low-mass slope at $z < 1$ to a downturned slope similar to the field at $z > 1$. Similarly, the highest density environments show a strong decrease of M^* with redshift at $z < 1$, becoming consistent with the field values at $z > 1$. Our study probes the redshift regime where these 'transitions' occur. Interestingly, we find that the core has an elevated M^* yet a field-like low α, and the rest of the cluster has a field-like M^* yet a steeper α more similar to that of the low redshift systems.

Physically, the radial dependence that our sample shows corresponds to the core having more high-mass quenched galaxies than the field, and the non-core regions having more low-mass galaxies than the field. From Figure 4.4, we see an increased quenched fraction from the field across both regimes, with the core having a highly increased quenched fraction. This high quenched fraction in the core, coupled with the varied similarity of the shapes of the star-forming and quiescent SMFs with the field, means that the total SMFs must also vary with environment. This is shown in Figure 5.2, where we present the SMFs of the core, the non-core, and the field. It shows that the non-core is most similar in form to the field, yet the core has a significantly different shape, with a highly increased high-mass portion. This highlights the differences of the populations in these environmental regimes.

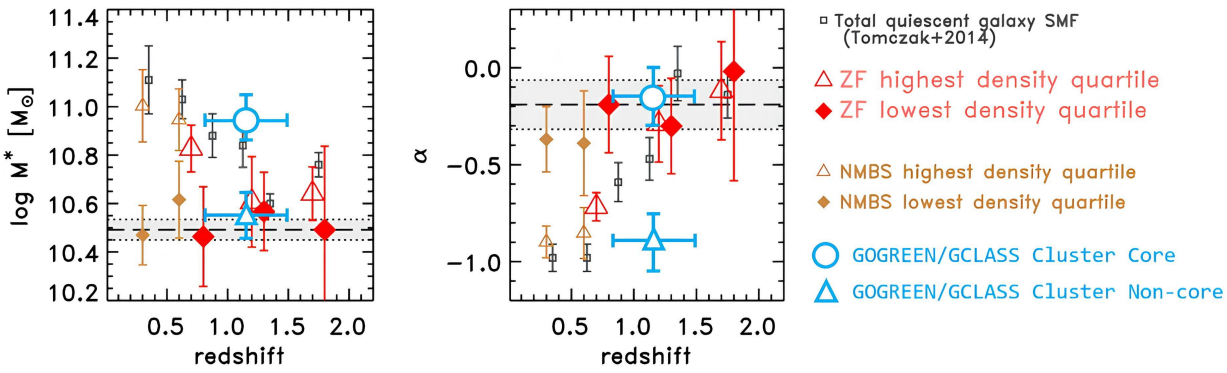


Figure 5.1: Adaption of Figure 4 in Papovich et al. (2018), showing the fit of the quiescent α and M^* values for the cluster core and the cluster non-core regions in our sample, compared to the results from ZFOURGE and NMBS in their work through a wide range of redshifts. We utilise the same symbol for our cluster non-core region as their 'highest density quartile' to emphasize the similarity of the environment of these two regimes. The grey shaded regions represent the mean range of parameter values for the 'lowest density quartile' environments.

5.2 Simple Quenching Pathway Model

As suggested by vdB20 and Webb et al. (2020), these results suggest two separate channels for increasing the quenched fraction in these clusters. Outside the core, a mildly enhanced quenched fraction appears consistent with expectations from a mass-independent environmental quenching of infalling star-forming galaxies, leading to a steeper α for the quenched population. On the other hand, the core appears to have a quiescent population more similar to the field, but with a much larger fraction of the total population. To demonstrate this, we create a simple model that explores the combination of quenching models that could lead to the quiescent populations we observe in each environment, as shown in Figures 5.3 and 5.4.

Similar to the experiment in Papovich et al. (2018), we create a simple model which considers the cluster quiescent SMF to be a combination of the field quiescent SMF and the field star-forming SMF. In their work they apply various mass-dependent and independent quenching profiles to the star-forming SMF in order to explore the efficacy of the mass-independent environmental quenching model (Peng et al., 2010; Kovač et al., 2014). In our model, we aim to explore the relative importance between the environmental quenching model from Peng et al. (2010) and the 'early mass quenching' model proposed in vdB20.

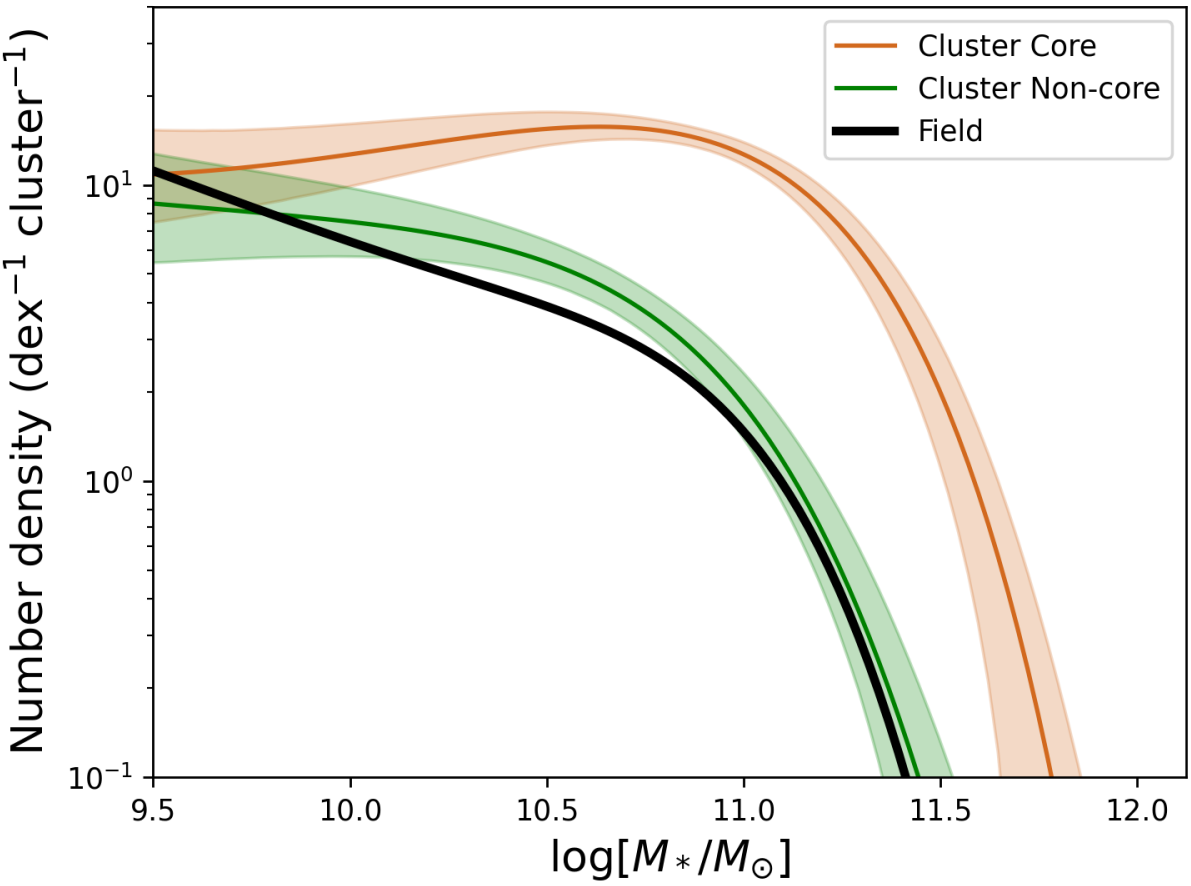


Figure 5.2: The combined total SMFs of the cluster core (brown) and the cluster outskirts (green) with their respective ± 1-σ errors. Also shown is the total field SMF evaluated from the fit parameters from McLeod et al. (2021). The figure highlights the similarity of the cluster non-core region with the field populations, and the significant difference of the cluster core population from them both.

We parameterize the importance of the early mass quenching model with the coefficient A_Q applied to the field quiescent SMF, and the importance of the environmental quenching model with the coefficient B_{SF} applied to the field star-forming SMF. The functional form of our model is given as

$$\phi(M)_{Q,C} = A_Q \phi(M)_{Q,F} + B_{SF} \phi(M)_{SF,F} \quad , \tag{5.1}$$

where $\phi(M)_{Q,C}$ is the cluster quiescent population, $\phi(M)_{Q,F}$ is the quiescent field population, and $\phi(M)_{SF,F}$ is the star-forming field population. The overall normalization of this combination is set by requiring the integral of $\phi(M)_{Q,C}$ to be equal to that of the observed data (or more specifically the parameterized fit). This ensures the total quenched fraction of our model matches that of the data, and means there is only one free parameter in our model (either A_Q or B_{SF}).

The top panel of Figure 5.3 shows the quiescent cluster core and three different model combination, each with increasing levels of environmental quenching (B_{SF} = 0.0, 0.1, 0.3). With the core having an α value consistent with the quiescent field value (see § 4.14), it is unsurprising that any major addition of an environmental quenching component will lead to a low-mass slope that diverges from the values observed in the cluster core. However, even in the case where the model is dominated entirely through early mass quenching (B_{SF} = 0.0), the model is unable to reproduce the high-mass quiescent population, which is due to the larger M^* value. In the bottom panel we explore similar field combinations, however, we assume the mass-quenched cluster population to be similar to that of the field. As such we allow the quiescent field to alter its M^* value along with its change in normalization. All model combinations increase the M^* by a factor of 0.24 dex, which is approximately the increase we see in the core from the field values (Figure 4.15). This is done to provide a more useful indication of how large an environmental quenching component can be tolerated by the data. We find with this change we are able to reproduce the observed SMF much better, in addition with models that include increased levels of environmental quenching ($B_{SF} \approx 0.25$) becoming more viable as well. In both of these panels, the value of A_Q is much higher than unity. This reflects the much higher quenched fraction in the cluster cores, and shows further that the quiescent core SMF has a similar shape to the field, but with a much higher normalization. This appears consistent with the interpretation of vdB20 and Webb et al. (2020), that the cluster core is dominated by quiescent galaxies that quenched similarly to the field, but with greater efficiency.

Figure 5.4 shows the equivalent experiment but evaluated for the cluster non-core region. For this population we find that without an environmental quenching component, the shape of the predicted SMF does not reproduce the observed trend, especially at the high-mass end. In the other two model combinations we decrease the early mass quenching

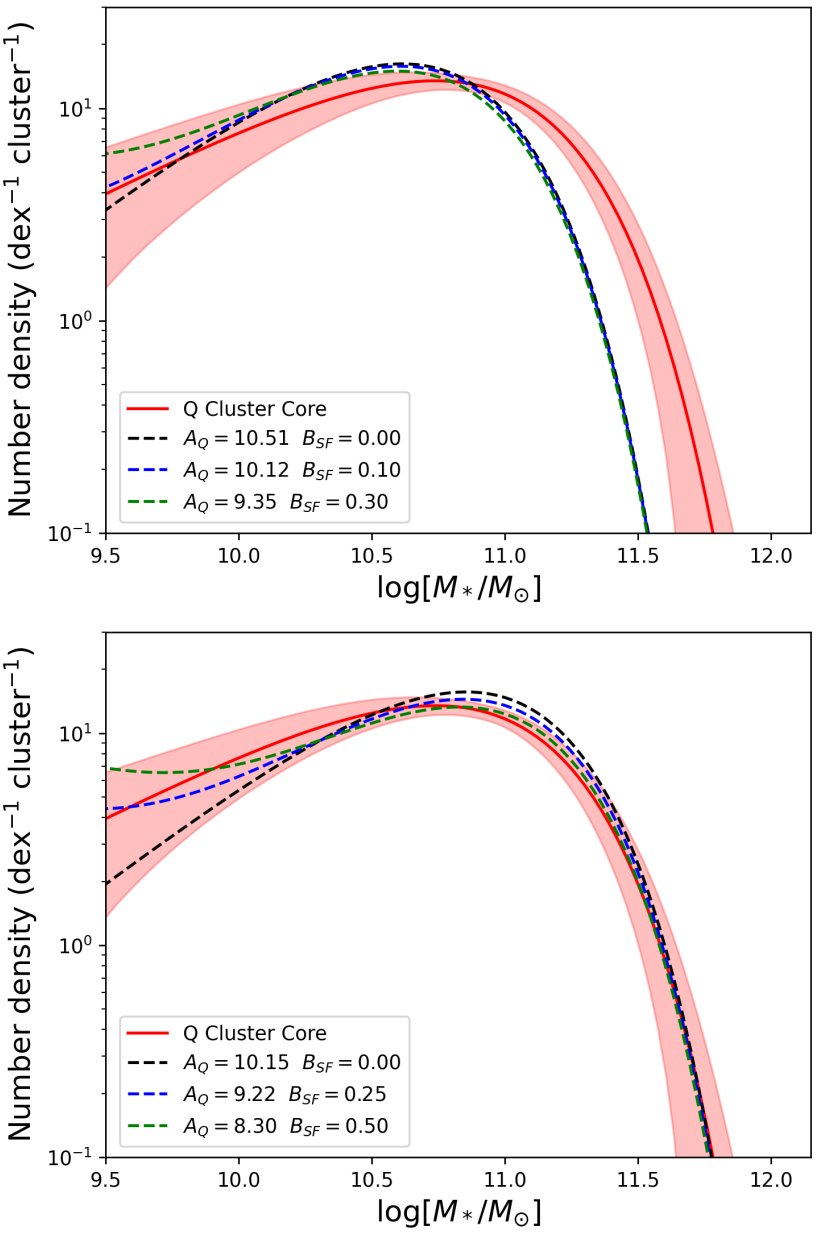


Figure 5.3: *Top*: Various combinations of the field star-forming and quiescent SMFs (coloured dashed curves) to replicate the form of the cluster core quiescent SMF (solid red curve with ± 1-σ errors). *Bottom*: Same as above but with the M^* value of the quiescent field SMF increased by 0.24 dex, to better show the degree of environmental quenching the model can include. The model parameters are constrained to match the normalization of the quiescent cluster population within our stellar mass range ($M_* > 10^{9.5} M_\odot$).

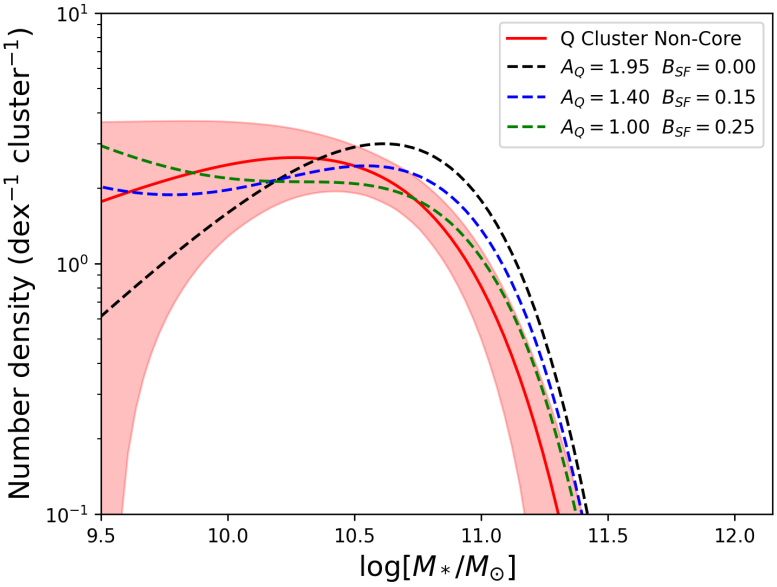


Figure 5.4: Various combinations of the field star-forming and quiescent SMFs (coloured dashed curves) to replicate the form of the cluster non-core quiescent SMF (solid red curve with $\pm$1-σ errors). The model parameters are constrained to match the normalization of the quiescent cluster population within our stellar mass range ($M_* > 10^{9.5} M_\odot$).

component, which allows for increased levels of environmental quenching. The model that contains only environmental quenching ($A_Q = 1.0$, $B_{SF} = 0.25$), does the best at reproducing both the low-mass and high-mass regimes of the observed SMF. This indicates that the non-core region is dominated by environmental quenching, and requires a minimal, if any, early mass quenching component.

5.3 Interpretation

The origin of quenched field galaxies (those produced through 'mass-quenching') is still a matter of ongoing research, but it is most likely due to AGN feedback (Croton et al., 2006; Hopkins et al., 2008; Fabian, 2012; Cicone et al., 2014; Bremer et al., 2018), perhaps fed in many cases by rich gas mergers (Kocevski et al., 2012; Fan et al., 2016; Mechtley et al., 2016; Shah et al., 2020). A natural interpretation of the enhanced quiescent population in our cluster core is therefore an enhanced efficiency of merger-driven AGN feedback. Tomczak et al. (2017) found this same massive quiescent galaxy excess within the highest density regimes of their sample (ZFOURGE), and explored models of galaxy-galaxy merging to help explain the discrepancy. Their merger model increased both the α and M^* values of their fits, allowing for better fits of the highest density populations.

The plausibility of mergers playing a role alongside early mass quenching increases with the evidence that the massive galaxies in the GOGREEN/GCLASS clusters were self-quenched or pre-processed prior to infall (Webb et al., 2020; Werner et al., 2022). The progenitors of cluster galaxies form within protoclusters, which simulations have shown to produce top-heavy initial mass functions and have enhanced specific star-formation rates (Chiang et al., 2017; Muldrew et al., 2018). Combined with moderate velocity dispersions that allow for significantly enhanced merger rates (Lotz et al., 2013), the conditions that protoclusters provide could explain both the mechanisms that allow for greater efficiency of early mass quenching, as well as increased presence of high-mass quenched galaxies.

The cluster non-core regions follow a quenching model more similar to that in Peng et al. (2010), due to the galaxies being more representative of the low density field population, where pre-processing in the protocluster environment would not be as prevalent. In addition, the buildup of the intracluster medium (ICM) creates an environment that allows for the typical mass-independent environmental quenching processes (e.g. ram-pressure stripping, strangulation) to become more efficient. However, the efficiencies of these processes are proportional to the local density of the ICM, and so it is expected that these processes would be more efficient in the cluster core. This is demonstrated in the bottom panel of Figure 5.3, with the model combinations in the core allowing for a larger range of

environmental quenching over the non-core, even though it is dominated by the enhanced mass quenching component.

5.4 Future Work

A key point that was missing from structure of the SMF fits was that the models were fit directly to the observed data, not the intrinsic form. It is common to include Eddington bias (Eddington, 1913) into SMF modelling to mitigate stellar mass errors, which can affect the shape of the mass functions at locations of steep dropoffs. If included, this would potentially increase the size of the posterior uncertainties, and shift the fit values for α and M^*, but the relative difference of M^* values through the cluster environment should remain the same. It should also be noted however, that the comparison field values used from McLeod et al. (2021) were of their own observed fits, rather than their intrinsic fits.

Many of the limitations in this project were due to sample size. The combination of the lower number of clusters in the sample, and the large cluster-to-cluster variation (e.g. Figures 4.5 and 4.6) made it difficult to constrain parameter values in our model that could consistently describe the entire sample. The project would benefit immensely from an increased sample size. The model described in this project is robust and efficient enough to explore additional relationships and parameterizations of the evolution of cluster SMFs. Using data from the upcoming large-field surveys from telescopes such as Euclid and LSST would allow this to occur. While it is true the project benefited from the depth the clusters were observed at, and these telescopes would not be able to achieve similar conditions, this could be overcome by exploring the local universe and smaller redshift regimes, which would also benefit the results with the increased redshift range that would provide.

The depth of the sample is still important however. One of the reasons why the α parameter in our model fits was not well constrained was that our completeness limits terminated in a stellar mass range where α could have a lot of variation. The equivalent quiescent field SMFs from McLeod et al. (2021) which were used extensively through this work, had fit functional forms at the redshift range of our sample where the upturn occurred just below our limit of $M_* > 10^{9.5} M_\odot$. Probing deeper would allow the model to explore and constrain this effect. It would potentially require the model to be redefined as a double Schechter function, but the core form described here would remain the same.

A major problem that plagues other similar works is increased membership error due to the extensive use of photometric redshifts. Our final sample had $\sim$ 40% of cluster

members with spectroscopic redshifts, and we were able to build off of these measurements to calibrate a statistical membership correction for the sample (see § 2.3.1). Euclid will effectively, and LSST will only have photometric measurements for the objects that they observe, but this could be mitigated by combining samples with measurements from instruments such as the Dark Energy Spectroscopic Instrument (DESI), the Mauna Kea Spectrographic Explorer (MSE), and ESO's Multi-Object Optical and Near-infrared Spectrograph (MOONS).

As previously discussed, the large variation in the global quenched fraction of the cluster sample as a function of redshift and cluster velocity dispersion indicates there are other dependencies that are primarily driving this scatter. As such there is a need to explore additional quenching dependencies within clusters. As seen within Figure 4.6, the use of velocity dispersion as a proxy for halo mass is hindered due to the large errors. The use of other methods to measure halo mass, such as galaxy-galaxy lensing, and using X-ray emission from the ICM, should be explored. Since the ICM is in part heated through the virialization of clusters, this could lead to the use of formation time or the age of the clusters as another quenching property to explore. Since determining the dynamical state of clusters through X-rays would require very high quality observations, one could make use of some alternative optical proxies, which look at the velocity and phase-space profiles (Roberts et al., 2018; Yu et al., 2018). Other additional variables to explore would be the gas fraction and metallicity of the cluster members, which would indicate the availability and cooling timescales of the gas in the galaxies. This could also allow for insight into the specific physical quenching mechanisms, which as discussed in § 1, could also be achieved with morphological information of the cluster members. All of these additional avenues would require extensive imaging and spectroscopic observations in order to attain the necessary population sizes and resolution, especially with these higher-redshift clusters.

A major conclusion we make in this work is that protoclusters have a significant effect on shaping the SMFs of clusters within the redshift range of our sample. A clear project extension would be to not only parameterize the SMFs of protoclusters at high redshifts, but also explore some of the additional cluster properties discussed above. This would allow for the observation of the buildup of massive quenched galaxies which become the progenitors of the cluster core galaxies, and in turn explore the potential mechanisms that are causing them to quench. Observations of increased merger rates as well as enhanced AGN fractions would help with the understanding of the results from this work. This would add to the current body of previous works, which have found evidence of elevated mass quenched populations within protoclusters (Muldrew et al., 2018; Hill et al., 2022; Edward et al., 2024).

Chapter 6

Summary and Conclusions

In this work we measure the SMFs down to a mass limit of $\log(M/M_{\odot}) = 9.5$ for seventeen rich galaxy clusters in the redshift range of $0.8 < z < 1.5$ from the GOGREEN and GCLASS surveys. We parameterize the α and M^* parameters to be themselves functions of cluster-centric radius and redshift, and parameterize the quenched fraction to be a function of redshift and cluster velocity dispersion. We compare our results with an equivalent field sample, and model the contribution of environmental quenching models for the quiescent populations at two radial regions. Our main findings are:

- There is a significant mass and radial dependency of the quenched fraction. The quenched fraction increases strongly with galaxy stellar mass and proximity to the cluster core, with the quenched fractions being larger than field values (McLeod et al., 2021) for all mass and radial values, with the core having highly elevated values (Figures 4.3 and 4.4). This is consistent with the results previously found with portions of the same data (Muzzin et al., 2012; van der Burg et al., 2020; Baxter et al., 2023).
- There is a weak, low-significance trend of decreasing quenched fraction with redshift, and no dependence of quenched fraction on cluster velocity dispersion (Figures 4.5 and 4.6). There are large quenched fraction cluster-to-cluster scatter as a function of these variables.
- The star-forming SMF fits show no radial or redshift dependence, and are consistent with field values (Figures 4.9 and 4.10).

- The quiescent SMF fits show no significant evidence for redshift dependence, and moderately significant evidence for radial dependence (Figures 4.12, 4.13, 4.14, and 4.15).

- The cluster core has a highly elevated quenched fraction dominated by high-mass quiescent galaxies, with a SMF more similar in shape to the quiescent field. This is indicative of an 'early mass quenching' model proposed in vdB20 (Figure 5.3). The cluster non-core region has an elevated quenched fraction dominated by low-mass quiescent galaxies, more similar in shape to the star-forming field. This is indicative of a mass-independent 'environmental quenching' model proposed in Peng et al. (2010) (Figure 5.4).

In conclusion, within these clusters we are seeing the first signs of environmental quenching mechanisms becoming the dominant quenching mechanisms of cluster member galaxies. Overall, however, the high quenched fraction relative to the field is dominated by the core population, which appears to have formed through an accelerated mass-quenching mechanism similar to what occurs for central galaxies. Future studies based on larger samples at lower and higher redshifts (e.g. from Euclid and LSST), combined with accurate redshift values (e.g. from DESI, MSE, and MOONS), should be able to probe the transition of dominant quenching models from protoclusters to massive low redshift clusters.

References

Abadi M. G., Moore B., Bower R. G., 1999, MNRAS, 308, 947

Annunziatella M., et al., 2014, A&A, 571, A80

Baldry I. K., Glazebrook K., Brinkmann J., Ivezić Ž., Lupton R. H., Nichol R. C., Szalay A. S., 2004, ApJ, 600, 681

Baldry I. K., Balogh M. L., Bower R. G., Glazebrook K., Nichol R. C., Bamford S. P., Budavari T., 2006, MNRAS, 373, 469

Balogh M. L., Morris S. L., 2000, MNRAS, 318, 703

Balogh M. L., Navarro J. F., Morris S. L., 2000, ApJ, 540, 113

Balogh M., et al., 2004a, MNRAS, 348, 1355

Balogh M. L., Baldry I. K., Nichol R., Miller C., Bower R., Glazebrook K., 2004b, ApJL, 615, L101

Balogh M. L., et al., 2016, MNRAS, 456, 4364

Balogh M. L., et al., 2017, MNRAS, 470, 4168

Balogh M. L., et al., 2021, MNRAS, 500, 358

Bartelmann M., 1996, A&A, 313, 697

Baxter D. C., et al., 2022, MNRAS, 515, 5479

Baxter D. C., et al., 2023, MNRAS, 526, 3716

Bekki K., 2014, MNRAS, 438, 444

Bertin E., Arnouts S., 1996, A&AS, 117, 393

Bialas D., Lisker T., Olczak C., Spurzem R., Kotulla R., 2015, A&A, 576, A103

Biviano A., et al., 2013, A&A, 558, A1

Biviano A., et al., 2021, A&A, 650, A105

Blumenthal G. R., Faber S. M., Primack J. R., Rees M. J., 1984, Nature, 311, 517

Bocquet S., Heitmann K., Habib S., Lawrence E., Uram T., Frontiere N., Pope A., Finkel H., 2020, ApJ, 901, 5

Bond J. R., Kofman L., Pogosyan D., 1996, Nature, 380, 603

Borgani S., Diaferio A., Dolag K., Schindler S., 2008, SSR, 134, 269

Boselli A., et al., 2016, A&A, 596, A11

Bremer M. N., et al., 2018, MNRAS, 476, 12

Brinckmann T., Lindholmer M., Hansen S., Falco M., 2016, JCAP, 2016, 007

Bundy K., et al., 2006, ApJ, 651, 120

Bundy K., Leauthaud A., Saito S., Maraston C., Wake D. A., Thomas D., 2017, ApJ, 851, 34

Burkert A., 1995, ApJL, 447, L25

Carroll S. M., 2001, Living Reviews in Relativity, 4, 1

Carroll S. M., Press W. H., Turner E. L., 1992, ARA&A, 30, 499

Cautun M., van de Weygaert R., Jones B. J. T., Frenk C. S., 2014, MNRAS, 441, 2923

Chiang Y.-K., Overzier R. A., Gebhardt K., Henriques B., 2017, ApJL, 844, L23

Cicone C., et al., 2014, A&A, 562, A21

Clauset A., Shalizi C. R., Newman M. E. J., 2009, SIAM Review, 51, 661

Cole S., 1991, ApJ, 367, 45

Contini E., Gu Q., Ge X., Rhee J., Yi S. K., Kang X., 2020, ApJ, 889, 156

Cowie L. L., Songaila A., Hu E. M., Cohen J. G., 1996, AJ, 112, 839

Croton D. J., et al., 2006, MNRAS, 365, 11

Cybulski R., Yun M. S., Fazio G. G., Gutermuth R. A., 2014, MNRAS, 439, 3564

Daddi E., et al., 2007, ApJ, 670, 156

De Lucia G., Blaizot J., 2007, MNRAS, 375, 2

Dekel A., Silk J., 1986, ApJ, 303, 39

Demarco R., et al., 2010, ApJ, 711, 1185

Dressler A., 1980, ApJ, 236, 351

Eddington A. S., 1913, MNRAS, 73, 359

Edward A. H., et al., 2024, MNRAS, 527, 8598

Einasto J., Kaasik A., Saar E., 1974, Nature, 250, 309

Elbaz D., et al., 2007, A&A, 468, 33

Fabian A. C., 2012, ARA&A, 50, 455

Fan L., et al., 2016, ApJL, 822, L32

Fontana A., et al., 2006, A&A, 459, 745

Foreman-Mackey D., 2016, The Journal of Open Source Software, 1, 24

Foreman-Mackey D., Hogg D. W., Lang D., Goodman J., 2013, PASP, 125, 306

Gamow G., Teller E., 1939, Physical Review, 55, 654

Gavazzi G., Fumagalli M., Cucciati O., Boselli A., 2010, A&A, 517, A73

Gilbank D. G., Balogh M. L., 2008, MNRAS, 385, L116

González V., Labbé I., Bouwens R. J., Illingworth G., Franx M., Kriek M., Brammer G. B., 2010, ApJ, 713, 115

Guglielmo V., et al., 2019, A&A, 625, A112

Gunn J. E., Gott J. Richard I., 1972, ApJ, 176, 1

Hill R., et al., 2022, MNRAS, 512, 4352

Höller H., Stöckl J., Benson A., Haider M., Steinhauser D., Lovisari L., Pranger F., 2014, A&A, 569, A31

Hopkins A. M., Beacom J. F., 2006, ApJ, 651, 142

Hopkins P. F., Hernquist L., Cox T. J., Kereš D., 2008, ApJS, 175, 356

Hopkins P. F., Quataert E., Murray N., 2012, MNRAS, 421, 3522

Hubble E., Humason M. L., 1931, ApJ, 74, 43

Ilbert O., et al., 2010, ApJ, 709, 644

Ilbert O., et al., 2013, A&A, 556, A55

Jeans J. H., 1902, Philosophical Transactions of the Royal Society of London Series A, 199, 1

Jenkins A., Frenk C. S., White S. D. M., Colberg J. M., Cole S., Evrard A. E., Couchman H. M. P., Yoshida N., 2001, MNRAS, 321, 372

Jian H.-Y., et al., 2017, ApJ, 845, 74

Kauffmann G., et al., 2003, MNRAS, 341, 54

Kauffmann G., White S. D. M., Heckman T. M., Ménard B., Brinchmann J., Charlot S., Tremonti C., Brinkmann J., 2004, MNRAS, 353, 713

Kawinwanichakij L., et al., 2017, ApJ, 847, 134

Kawinwanichakij L., et al., 2020, ApJ, 892, 7

Khochfar S., Silk J., 2009, MNRAS, 397, 506

Klypin A., Yepes G., Gottlöber S., Prada F., Heß S., 2016, MNRAS, 457, 4340

Kocevski D. D., et al., 2012, ApJ, 744, 148

Kovač K., et al., 2014, MNRAS, 438, 717

Larson R. B., Tinsley B. M., Caldwell C. N., 1980, ApJ, 237, 692

Leethochawalit N., Kirby E. N., Ellis R. S., Moran S. M., Treu T., 2019, ApJ, 885, 100

Łokas E. L., Mamon G. A., 2001, MNRAS, 321, 155

Lotz J. M., et al., 2013, ApJ, 773, 154

Lotz M., Dolag K., Remus R.-S., Burkert A., 2021, MNRAS, 506, 4516

Madau P., Dickinson M., 2014, ARA&A, 52, 415

Mahajan S., Haines C. P., Raychaudhury S., 2010, MNRAS, 404, 1745

Maier C., et al., 2016, A&A, 590, A108

Malumuth E. M., Kriss G. A., 1986, ApJ, 308, 10

Marchesini D., et al., 2014, ApJ, 794, 65

McLeod D. J., McLure R. J., Dunlop J. S., Cullen F., Carnall A. C., Duncan K., 2021, MNRAS, 503, 4413

McNab K., et al., 2021, MNRAS, 508, 157

Mechtley M., et al., 2016, ApJ, 830, 156

Merluzzi P., et al., 2013, MNRAS, 429, 1747

Moore B., Katz N., Lake G., Dressler A., Oemler A., 1996, Nature, 379, 613

Moustakas J., et al., 2013, ApJ, 767, 50

Muldrew S. I., Hatch N. A., Cooke E. A., 2018, MNRAS, 473, 2335

Muzzin A., et al., 2009, ApJ, 698, 1934

Muzzin A., et al., 2012, ApJ, 746, 188

Muzzin A., et al., 2013, ApJ, 777, 18

Oegerle W. R., Hoessel J. G., Ernst R. M., 1986, AJ, 91, 697

Ostriker J. P., Peebles P. J. E., Yahil A., 1974, ApJL, 193, L1

Padmanabhan T., 2003, Physics Reports, 380, 235

Papovich C., et al., 2018, ApJ, 854, 30

Peebles P. J. E., 1965, ApJ, 142, 1317

Peebles P. J., Ratra B., 2003, Reviews of Modern Physics, 75, 559

Peng Y.-j., et al., 2010, ApJ, 721, 193

Peng Y., Maiolino R., Cochrane R., 2015, Nature, 521, 192

Penzias A. A., Wilson R. W., 1965, ApJ, 142, 419

Pintos-Castro I., Yee H. K. C., Muzzin A., Old L., Wilson G., 2019, ApJ, 876, 40

Planck Collaboration et al., 2020, A&A, 641, A6

Press W. H., Schechter P., 1974, ApJ, 187, 425

Quilis V., Planelles S., Ricciardelli E., 2017, MNRAS, 469, 80

Reeves A. M. M., et al., 2021, MNRAS, 506, 3364

Roberts I. D., Parker L. C., Hlavacek-Larrondo J., 2018, MNRAS, 475, 4704

Roberts I. D., Parker L. C., Brown T., Joshi G. D., Hlavacek-Larrondo J., Wadsley J., 2019, ApJ, 873, 42

Rowe B. T. P., et al., 2015, Astronomy and Computing, 10, 121

Rudnick G., et al., 2009, ApJ, 700, 1559

Sales L. V., Navarro J. F., Peñafiel L., Peng E. W., Lim S., Hernquist L., 2020, MNRAS, 494, 1848

Sandage A., Tammann G. A., Yahil A., 1979, ApJ, 232, 352

Santini P., et al., 2017, ApJ, 847, 76

Sawicki M., 2012, MNRAS, 421, 2187

Schechter P., 1976, ApJ, 203, 297

Schwarz G., 1978, Annals of Statistics, 6, 461

Scoville N., et al., 2013, ApJS, 206, 3

Seppi R., et al., 2021, A&A, 652, A155

Shah E. A., et al., 2020, ApJ, 904, 107

Silk J., Rees M. J., 1998, A&A, 331, L1

Smit R., Bouwens R. J., Franx M., Illingworth G. D., Labbé I., Oesch P. A., van Dokkum P. G., 2012, ApJ, 756, 14

Smith R., Davies J. I., Nelson A. H., 2010, MNRAS, 405, 1723

Springel V., 2005, MNRAS, 364, 1105

Stott J. P., 2022, MNRAS, 511, 2659

Straatman C. M. S., et al., 2016, ApJ, 830, 51

Tinker J., Kravtsov A. V., Klypin A., Abazajian K., Warren M., Yepes G., Gottlöber S., Holz D. E., 2008, ApJ, 688, 709

Tomczak A. R., et al., 2014, ApJ, 783, 85

Tomczak A. R., et al., 2016, ApJ, 817, 118

Tomczak A. R., et al., 2017, MNRAS, 472, 3512

Tonnesen S., 2019, ApJ, 874, 161

Vaughan S. P., et al., 2020, MNRAS, 496, 3841

Vulcani B., et al., 2012, MNRAS, 420, 1481

Vulcani B., et al., 2013, A&A, 550, A58

Weaver J. R., et al., 2023, A&A, 677, A184

Webb K., et al., 2020, MNRAS, 498, 5317

Wechsler R. H., Tinker J. L., 2018, ARA&A, 56, 435

Weinmann S. M., van den Bosch F. C., Yang X., Mo H. J., 2006, MNRAS, 366, 2

Werner S. V., Hatch N. A., Muzzin A., van der Burg R. F. J., Balogh M. L., Rudnick G., Wilson G., 2022, MNRAS, 510, 674

Wetzel A. R., Tinker J. L., Conroy C., 2012, MNRAS, 424, 232

Whitaker K. E., et al., 2011, ApJ, 735, 86

White S. D. M., Frenk C. S., 1991, ApJ, 379, 52

White S. D. M., Rees M. J., 1978, MNRAS, 183, 341

Wilson G., et al., 2009, ApJ, 698, 1943

Yu H., Diaferio A., Serra A. L., Baldi M., 2018, ApJ, 860, 118

Zel'dovich Y. B., 1970, A&A, 5, 84

Zeldovich Y. B., 1972, MNRAS, 160, 1P

Zhang Y., et al., 2019, MNRAS, 488, 1

Zwicky F., 1933, Helvetica Physica Acta, 6, 110

Zwicky F., 1937, ApJ, 86, 217

van den Bosch F. C., Aquino D., Yang X., Mo H. J., Pasquali A., McIntosh D. H., Weinmann S. M., Kang X., 2008, MNRAS, 387, 79

van der Burg R. F. J., Hildebrandt H., Erben T., 2010, A&A, 523, A74

van der Burg R. F. J., et al., 2013, A&A, 557, A15

van der Burg R. F. J., McGee S., Aussel H., Dahle H., Arnaud M., Pratt G. W., Muzzin A., 2018, A&A, 618, A140

van der Burg R. F. J., et al., 2020, A&A, 638, A112

APPENDICES

Appendix A

Redshift Dependence Likelihood

During the construction of the likelihood in this work, we also validated the use of setting the normalization of the red population of each cluster as a free parameter, following the spirit of Zhang et al. (2019). The associated likelihood would be the probability of finding galaxy i of type $x = r, b$ in cluster cl (or equivalently at redshift z), denoted as $\mathcal{L}_{cl,i}$. With the formulation of this dependence, we wanted to make sure that the total number of galaxies in cluster cl is independent of the SMF parameters, and are instead constrained by the radial profiles. Using the definition of f_q that we set in 3.15, we end with a form of:

$$\begin{aligned} N_{cl} &= \int_0^{R_{\rm max,cl}} 2\pi R \Sigma_r^* \rho(c_{cl,r}, R) dR + \int_0^{R_{\rm max,cl}} 2\pi R \Sigma_b^* \rho(c_{cl,b}, R) dR \\ &= \frac{2\pi \Sigma_{cl,r}^*}{f_q(cl)} \int_0^{R_{\rm max,cl}} \rho(c_r, R) R dR. \end{aligned} \tag{A.1}$$

We structure the redshift likelihood in terms of a Poisson distribution. We parameterize the expected fraction of members in each cluster (μ) as equivalent to N_{cl}, and treat the real observed data ($N_{obs,cl}$) as a random draw from the distribution. This gives the form:

$$\begin{aligned} P(x, \mu) &= P\left(N_{obs,cl}, \frac{2\pi \Sigma_{cl,r}^*}{f_q(cl)} \int_0^{R_{\rm max,cl}} \rho(c_r, R) R dR\right) \\ &= \frac{e^{-\frac{\Sigma_{cl,r}^* 2\pi \int \rho(c_r,R) R dR}{f_q(cl)}} \left(\frac{\Sigma_{cl,r}^* 2\pi \int \rho(c_r,R) R dR}{f_q(cl)}\right)^{N_{obs,cl}}}{N_{obs,cl}!} = \mathcal{L}_{cl,i}. \end{aligned} \tag{A.2}$$

This would give a set of red population normalizations for each cluster $\{\Sigma_{cl,r}^*\}$ with length N matching the number of clusters in the sample. This increases the number of

parameters to $21+N$. The redshift dependence is implemented within the overall likelihood as an additional product:

$$\mathcal{L}_{i,x} = \mathcal{L}_{M,i,x} \times \mathcal{L}_{R,i,x} \times \mathcal{L}_{cl,i}. \tag{A.3}$$